Supplement of SOIL, 12, 497–519, 2026
https://doi.org/10.5194/soil-12-497-2026-supplement

Supplement of

Prediction of peat properties from transmission mid-infrared spectra

Henning Teickner and Klaus-Holger Knorr

Correspondence to: Henning Teickner (henning.teickner@uni-muenster.de)

Contents

Henning Teickner[1,2,*]
Klaus-Holger Knorr[1]

[1] Ecohydrology & Biogeochemistry Group, Institute of Landscape Ecology, University of Münster, 48149, Germany
[2] Spatiotemporal Modelling Lab, Institute for Geoinformatics, University of Münster, 48149, Germany
[*] corresponding author(s): Henning Teickner (henning.teickner@uni-muenster.de)

S1 Pedotransfer functions

S1.1 Total porosity, macroporosity

Total porosity is defined as the volume fraction of a peat sample which is filled either with gas or water. Macroporosity is defined, following Liu and Lennartz (2019), as the difference between total porosity and the volumetric water content at 60 cm pressure head (implying a pore diameter of ~ 50 µm).

The pmird database does not contain measured peat porosities and MIRS measured for the same samples. However, both can in principle be predicted from peat bulk density, even though prediction errors of such pedotransfer functions are large (Liu and Lennartz, 2019; Liu et al., 2020), especially in combination with prediction errors for bulk densities from the MIRS prediction model.

We nevertheless think that computing such models is useful because it is still better to have a rough estimate than no estimate, our approach provides software infrastructure to combine pedotransfer functions and spectral prediction models, and it is easier to test the usefulness of both the spectral prediction model and the pedotransfer function when such combined models are available.

The pmird database contains the data collected by Liu and Lennartz (2019) and we computed a modified version of their models for the volume fractions of different pore classes. Our model has the following structure:

$$
\begin{aligned}
\begin{bmatrix} y_{\text{macropores}} \\ y_{\text{non-macropores}} \\ y_{\text{solids}} \end{bmatrix} &\sim \text{Dirichlet}\left(\begin{bmatrix} \mu_{\text{macropores}} \\ \mu_{\text{non-macropores}} \\ \mu_{\text{solids}} \end{bmatrix}, \phi\right) \\
\mu_{\text{macropores}} &= \frac{\exp(\eta_{\text{macropores}})}{\sum_{k \in \{\text{macropores, non-macropores, solids}\}} \exp(\eta_k)} \\
\mu_{\text{non-macropores}} &= \frac{\exp(\eta_{\text{non-macropores}})}{\sum_{k \in \{\text{macropores, non-macropores, solids}\}} \exp(\eta_k)} \\
\mu_{\text{solids}} &= \frac{\exp(\eta_{\text{solids}})}{\sum_{k \in \{\text{macropores, non-macropores, solids}\}} \exp(\eta_k)} \\
\eta_{\text{macropores}} &= \alpha_{\text{macropores}} + \beta_{\text{1, macropores}} x + \beta_{\text{2, macropores}} \ln(x) \\
\eta_{\text{non-macropores}} &= \alpha_{\text{non-macropores}} + \beta_{\text{1, non-macropores}} x + \beta_{\text{2, non-macropores}} \ln(x) \\
\eta_{\text{solids}} &= 0 \\
\alpha_{\text{macropores}} &\sim \text{normal}(\mu_{\alpha_{\text{macropores}}}, \sigma_{\alpha_{\text{macropores}}}) \\
\alpha_{\text{non-macropores}} &\sim \text{normal}(\mu_{\alpha_{\text{non-macropores}}}, \sigma_{\alpha_{\text{non-macropores}}}) \\
\beta_{\text{1, macropores}} &\sim \text{normal}(\mu_{\beta_{\text{1, macropores}}}, \sigma_{\beta_{\text{1, macropores}}}) \\
\beta_{\text{2, macropores}} &\sim \text{normal}(\mu_{\beta_{\text{2, macropores}}}, \sigma_{\beta_{\text{2, macropores}}}) \\
\beta_{\text{1, non-macropores}} &\sim \text{normal}(\mu_{\beta_{\text{1, non-macropores}}}, \sigma_{\beta_{\text{1, non-macropores}}}) \\
\beta_{\text{2, non-macropores}} &\sim \text{normal}(\mu_{\beta_{\text{2, non-macropores}}}, \sigma_{\beta_{\text{2, non-macropores}}}) \\
\phi &\sim \text{gamma}(\alpha_\phi, \beta_\phi),
\end{aligned}
\tag{S1}
$$

where μ_{k} is the average volume fraction of compartment k, $k \in \{\text{macropores, non-macropores, solids}\}$, η_{k} is the same, but on the latent scale, $\alpha_{\text{macropores}}$, $\alpha_{\text{non-macropores}}$, $\beta_{\text{1, macropores}}$, $\beta_{\text{2, macropores}}$, $\beta_{\text{1, non-macropores}}$, and $\beta_{\text{2, non-macropores}}$ are the intercept and slopes to model the average volume fraction of macropores and non-macropores from the bulk density (x), respectively, which are modeled with normal prior distributions, and ϕ is the precision parameter of the Dirichlet distribution, assumed to have a gamma distribution. Solids serve as reference class and therefore have $\eta_{\text{solids}} = 0$.

The modifications are the following:

1. Instead of modelling macroporosity and non-macroporosity separately, we model them simultaneously using a Dirichlet regression model which also models the volume fraction of solids. This considers that the volume fractions of macropores, non-macro pores, and solid matter each cannot be smaller than 0% or larger than 100% and must sum to 100%.

2. Instead of using simple linear or exponential relations of each class with bulk density,

we model macroporosity and non-macroporosity with a Ricker-like model (Ricker, 1954), i.e. $\eta_k = \alpha + x\beta_{1,k} + \ln(x)\beta_{2,k}$. Apart from better fitting the data than a simple linear or exponential model, a Ricker-like model makes intuitively sense:

- A reasonable assumption is that the total porosity must decrease with increasing bulk density, as shown in Liu and Lennartz (2019) and also observable for organic shales (extremely compacted organic sediments, see modification 3 below) (Wang et al., 2015), because otherwise one would have to assume that the total porosity could increase or remain constant while the bulk density increases, which would only be possible if low density solids would be replaced by high density solids without changing or while increasing the total porosity — an unlikely scenario. The $\ln(x)\beta_{2,k}$ terms account for this assumption.
- Peat mass loss during decomposition is assumed to be proportional to the remaining mass and therefore can be modeled with an exponential function (e.g., Clymo, 1984). Similarly, we assume that the loss of macropores is proportional to the fraction of remaining macropores because more macropores imply more fibers which form the boundaries of macropores and these fibers get decomposed by losing mass. If one then assumes that the loss of macropores occurs at a higher rate than the loss of peat mass — because compaction happens faster than mass loss — this implies a decreasing exponential relation of macroporosity with bulk density, as shown in Liu and Lennartz (2019). The $x\beta_{1,k}$ term account for this.
- This relatively simple model can also account for the decrease in non-macroporosity with increasing bulk densities (Fig. S1).
- When the bulk density approaches zero, a sample is in principle the content of a container filled with gas, i.e. the sample is a single macropore (if one considers a sample with sufficiently large volume). The model is in accordance with this because at a very small bulk density, it predicts a macroporosity of 100%, a non-macroporosity of 0%, and a fraction of solids of 0%. Likewise, for very high bulk densities, the model predicts a macroporosity of 0%, a non-macroporosity of 0%, and a fraction of solids of 100% (Fig. S1).

3. We added data from organic shales extracted from table 2 in Wang et al. (2015) to the model. As described above, organic shales may be formed from peat-like material due to extreme compaction (Wang et al., 2015) and a model which captures the general relation between porosity and bulk density, should also fit data for organic shales as one extreme (high bulk density and low porosity) (Wang et al., 2015). Including such high-bulk density data allows us to make the assumption that this model can be applied both to very low-density, but also very high-density peat samples.
   The porosity values reported by Wang et al. (2015) represent total porosities and no easily extractable data for the macroporosity and non-macroporosity are given. Since the fraction of macropores in these organic shales is small (see Fig. 5 in Wang et al. (2015)), we assumed a macroporosity of 0% or, equivalently, that the porosity data reported equals the non-macroporosity.

In accordance with the theoretical justifications, we chose prior distributions for the intercept that reflect that the macroporosity should be 100%, the non-macroporosity 0%, and the fraction of solids 0% when the bulk density goes to 0 g cm^{-3}. For all other parameters, we used weakly informative priors. Model fits to the data are shown in Fig. S2. As additional test, we compared model predictions for total porosity to measurements by Whittington and Koiter (2024). Predictions of our model agree within prediction interval boundaries to the measured values (Fig. S3).

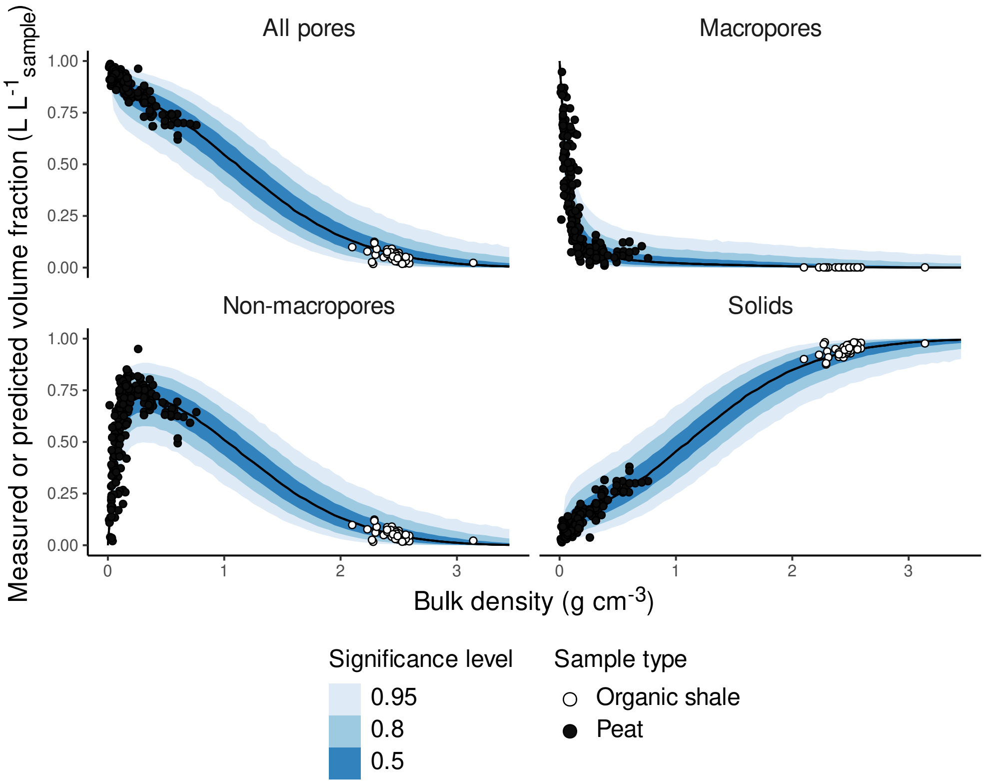

Figure S1: Plot of measured (points) and predicted (lines and shaded areas) total porosity, macroporosity, non-macroporosity, and volume fraction of solids versus bulk density. Shaded areas are prediction intervals. Data from organic shales are from Wang et al. (2015) and data from peat samples are from Liu and Lennartz (2019) as contained in the pmird database.

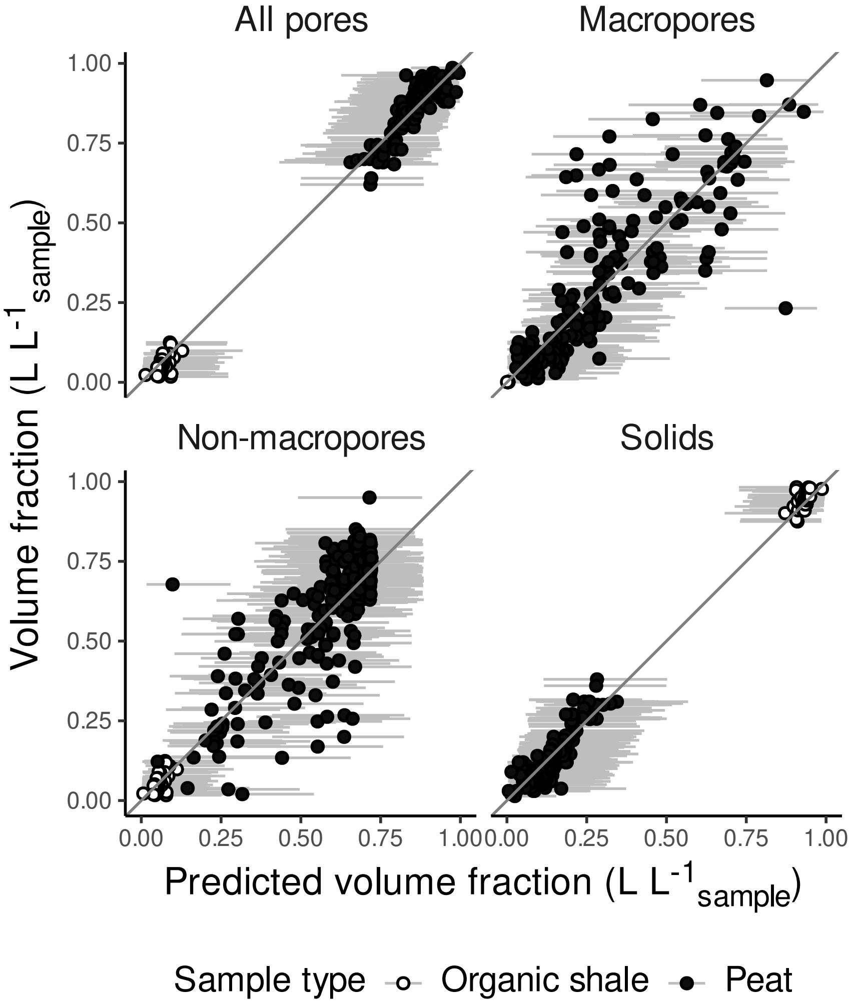

Figure S2: Plot of measured (or assumed) total porosity, macroporosity, non-macroporosity, and volume fraction of solids versus predictions by model (S1). Error bars are 95% prediction intervals.

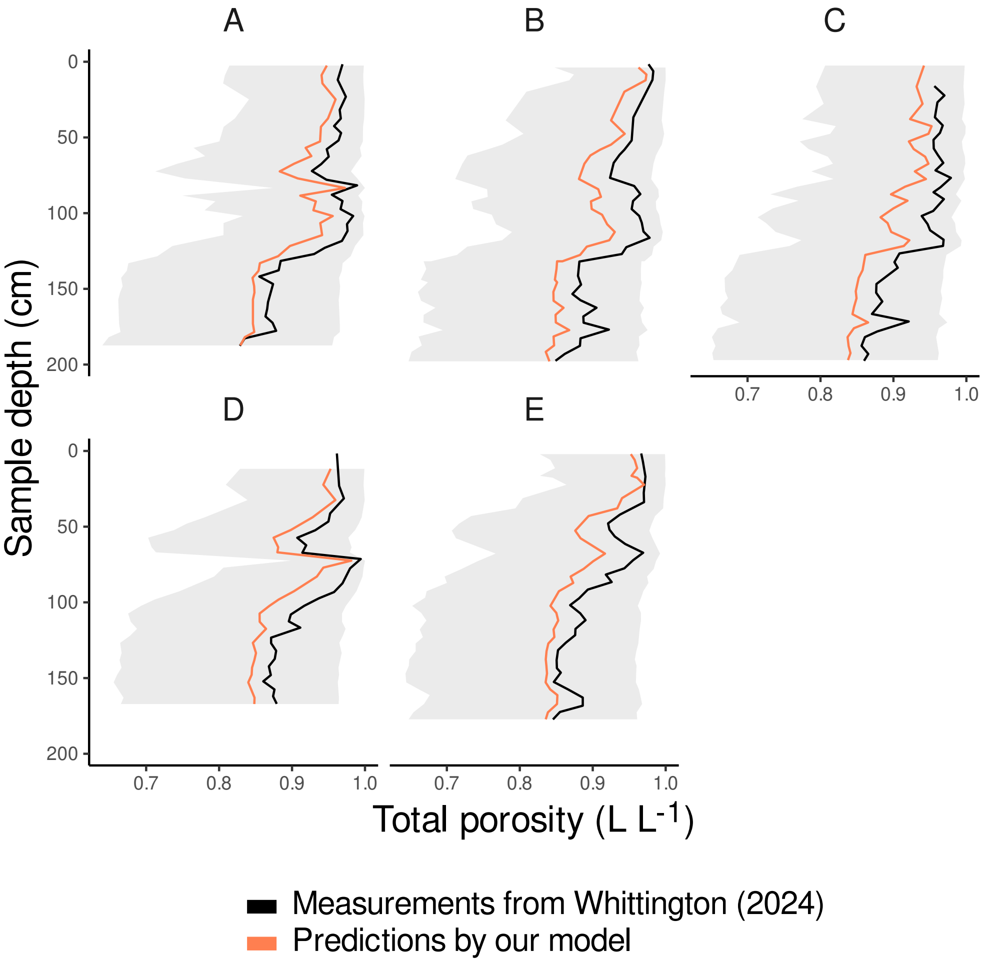

Figure S3: Comparison of model predictions for total porosity to measured total porosities for peat cores from Whittington and Koiter (2024). Each panel shows values for one peat core. Lines are averages. Shaded areas are 95% prediction intervals.

S1.2 Saturated hydraulic conductivity (K_s)

As for porosity, the pmird database does not contain measured peat saturated hydraulic conductivity (K_s) and MIRS measured for the same samples, but pedotransfer functions are available to predict it from bulk densities (Liu and Lennartz, 2019). To predict K_s from MIRS, we used the same strategy as for porosity, again recomputing modified versions of the model described in Liu and Lennartz (2019).

Values of K_s are highly variable for small bulk densities (Liu and Lennartz, 2019) because they do not just depend on porosity, but also factors such as pore connectivity. However, peat with a small fraction of macropores (or equivalently a bulk density approximately > 0.15 g cm^{-3}) generally has a small K_s (Liu and Lennartz, 2019). The simple model we present therefore is informative in so far as it makes accurate predictions when K_s is small, but it does not provide very accurate estimates for peat with bulk densities approximately ≤ 0.15 g cm^{-3}. As described for porosity above, we nevertheless think that it is useful to compute such a model.

Again, we modified the original model for K_s to model K_s on the original scale (not log-scaled). In addition, we modeled K_s with a beta regression model, assuming that K_s is in (0, 3000) cm h^{-1} (Liu and Lennartz, 2019). This has mainly the advantage to restrict the maximum error ranges in comparison to using a gamma distribution:

$$\begin{aligned}
K_s \sim &\quad \text{beta}(\mu\phi, (1-\mu)\phi) \\
\mu = &\quad \frac{1}{1+\exp(-\eta)} \\
\eta = &\quad \alpha_\mu + \beta_{1,\mu} x + \beta_{2,\mu} \ln(x) \\
\alpha_\mu \sim &\quad \text{normal}(\mu_{\alpha_\mu}, \sigma_{\alpha_\mu}) \\
\beta_{1,\mu} \sim &\quad \text{normal}(\mu_{\beta_{1,\mu}}, \sigma_{\beta_{1,\mu}}) \\
\beta_{2,\mu} \sim &\quad \text{normal}(\mu_{\beta_{2,\mu}}, \sigma_{\beta_{2,\mu}}) \\
\phi = &\quad \exp(\alpha_\phi + \beta_{1,\phi} x + \beta_{2,\phi} \ln(x)) \\
\alpha_\phi \sim &\quad \text{normal}(\mu_{\alpha_\phi}, \sigma_{\alpha_\phi}) \\
\beta_{1,\phi} \sim &\quad \text{normal}(\mu_{\beta_{1,\phi}}, \sigma_{\beta_{1,\phi}}) \\
\beta_{2,\phi} \sim &\quad \text{normal}(\mu_{\beta_{2,\phi}}, \sigma_{\beta_{2,\phi}}),
\end{aligned} \tag{S2}$$

where μ is the average saturated hydraulic conductivity, ϕ the precision parameter of the beta distribution, α_μ, $\beta_{1,\mu}$, and $\beta_{2,\mu}$ are the intercept and slopes for the model for μ in dependency of the bulk density (x), all modeled with normal prior distributions, and α_ϕ and β_ϕ are the intercept and slope for the model for ϕ in dependency of the bulk density, which are also modeled with normal prior distributions.

Since K_s depends on porosity, we used the same model for the average bulk density, i.e. $\mu = \alpha + \beta_1 x + \beta_2 \log(x)$ (see above). Also the variability in K_s (modeled by ϕ) is related to bulk density and therefore we included a model term for ϕ in dependency of the bulk density in the model. Since one can expect that K_s is similarly small for peat with even higher bulk densities than contained in the data from Liu and Lennartz (2019), we assume that this model can be used across the full range of bulk densities for peat. Plots of measured and predicted K_s versus bulk density are shown in Fig. S4 and measurements versus fitted values in Fig. S5. As additional test, we compared model predictions to measurements by Whittington and Koiter (2024) and predictions of model 1 from Morris et al. (2022) (Fig. S3). Predictions of our model agree within prediction interval boundaries to the measured values, but the predicted average is larger than the measurements and our predictions agree better with predictions from model 1 from Morris et al. (2022) than with measurements from Whittington and Koiter (2024).

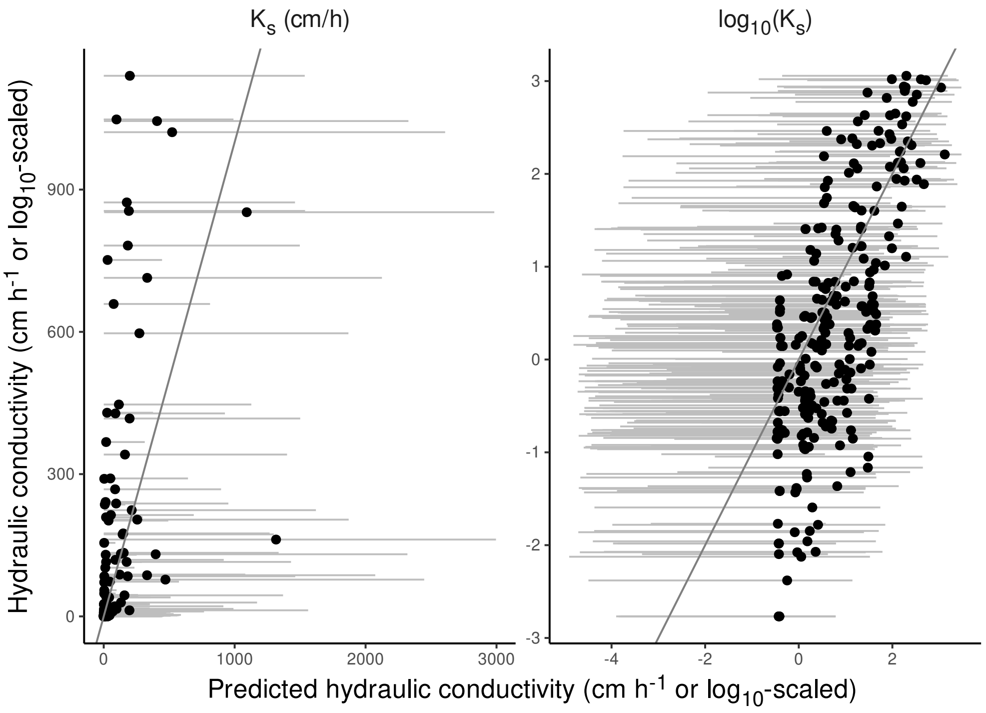

Figure S4: Plot of measured K_s versus predictions by model (S2), either on the raw scale or the $\log_{10}$-transformed values. Error bars are 95% prediction intervals.

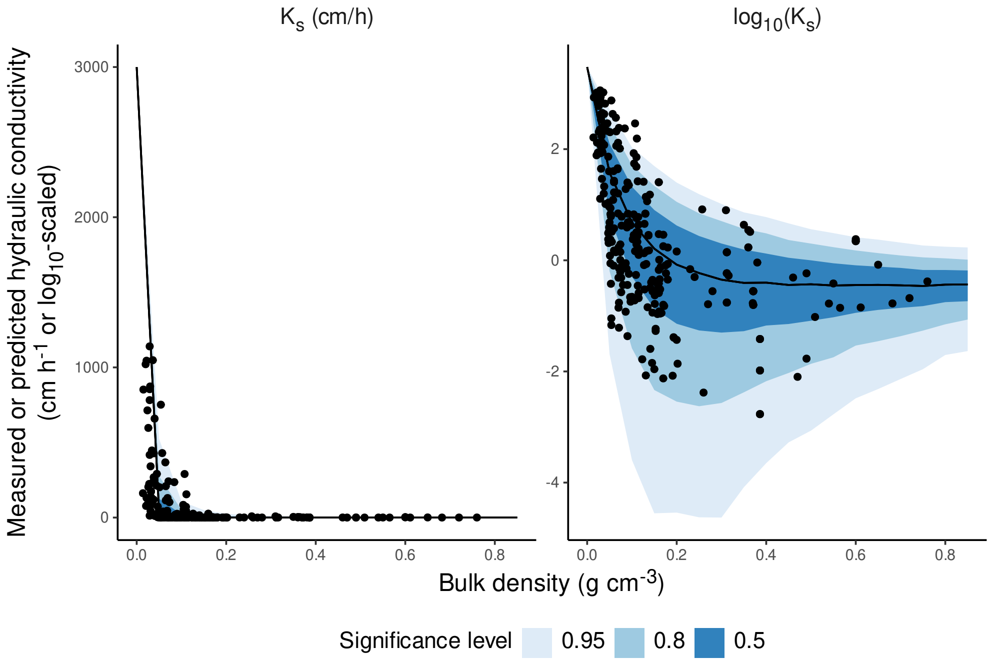

Figure S5: Plot of measured (points) and predicted (lines and shaded areas) K_s, either on the raw scale or the $\log_{10}$-transformed values. Shaded areas are prediction intervals.

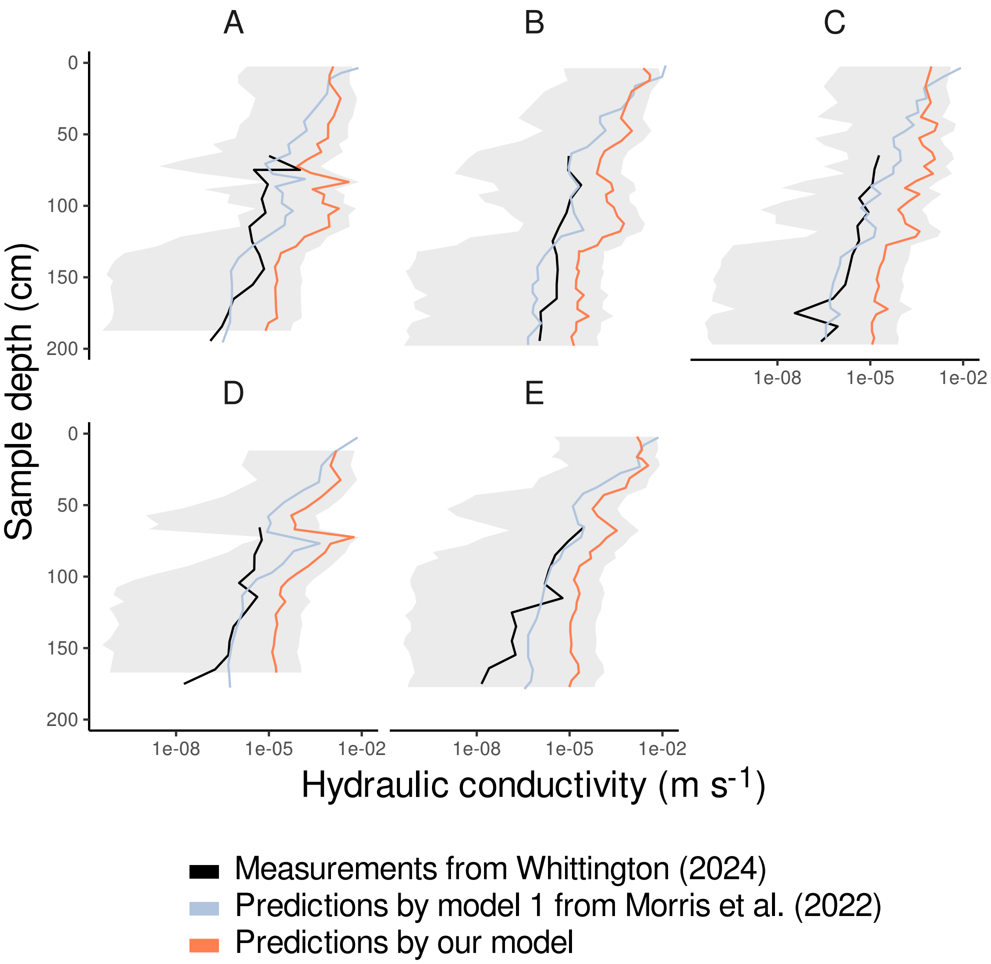

Figure S6: Comparison of model predictions for saturated hydraulic conductivity to measured saturated hydraulic conductivity for peat cores from Whittington and Koiter (2024) and saturated hydraulic conductivity predicted for the same cores with model 1 from Morris et al. (2022). Each panel shows values for one peat core. Lines are averages. Shaded areas are 95% prediction intervals.

S1.3 Specific heat capacity (c_p)

The pmird database does not contain measured peat specific heat capacities and MIRS measured for the same samples. However, peat specific heat capacities can be modeled from peat N contents if the peat temperature is known (Gnatowski et al., 2022).

We therefore modeled the specific heat capacity from MIRS by predicting peat N contents from MIRS and then using the approach described in Gnatowski et al. (2022). We recomputed the models described there with the reported data and some modifications:

$$
\begin{aligned}
c_{p,\text{measured}} &\sim \text{normal}(c_p, \sigma_{c_p}) \\
c_p &\sim \text{gamma}\left(\phi, \frac{\phi}{\mu_{c_p}}\right) \\
\mu_{c_p} &= \exp(\alpha_{C_0}[i] + \beta_{C_0}\text{N} + \alpha_{C_1}\text{T} + \beta_{C_1}\text{NT}) \\
\alpha_{C_0}[i] &\sim \text{normal}(\alpha, \sigma) \\
\sigma &\sim \text{normal}^+(0, 0.2) \\
\phi &\sim \text{gamma}(1, 0.005),
\end{aligned}
\tag{S3}
$$

where c_p is the true specific heat capacity (J g^{-1} K^{-1}), $c_{p,\text{measured}}$ the measured specific heat capacity (J g^{-1} K^{-1}) with reported measurement errors σ_{c_p} (Gnatowski et al., 2022), μ_{c_p} the expected value of the specific heat capacity (J g^{-1} K^{-1}), $\alpha_{C_0}[i]$ is μ_{c_p} for T = 0 K and a solid N content of 0 mass-% (equivalent to the intercept for C_0 in Gnatowski et al. (2022)), β_{C_0} describes how μ_{c_p} changes with N content (equivalent to the slope for C_0 in Gnatowski et al. (2022)), α_{C_1} is the change in μ_{c_p} with temperature (equivalent to the intercept for C_1 in Gnatowski et al. (2022)), β_{C_1} describe how μ_{c_p} changes with temperature and N content (equivalent to the slope for C_1 in Gnatowski et al. (2022)). α and σ are the global intercept and standard deviation for the $\alpha_{C_0}[i]$, to account for the repeated measurements per sample. The modifications consider that $c_p > 0$ J g^{-1} K^{-1} (gamma distribution), propagate errors in C_0 and C_1 as predicted from N content to c_p, and consider measurement errors in c_p. In addition, to account for repeated measurements of the heat capacity for each peat sample at different temperatures, we model $\alpha_{C_0}[i]$ with a normal distribution with global intercept α and standard deviation σ. Parameter α was set to $\log(c_p(\text{air}))$, where $c_p(\text{air})$ is the specific heat capacity of dry air at 0 K.

The data in Gnatowski et al. (2022) are from drained peat and therefore are not representative for less decomposed peat. To extent the model to less decomposed peat, we use data for the specific heat capacity of dry air from Hilsenrath et al. (1955). Undecomposed peat is known to have lower N contents and larger pore spaces. The larger the porosity is the more is the specific heat capacity of dry peat controlled by that of the enclosed air. Therefore, we used the data for the specific heat capacity of dry air as estimate for the specific heat capacity of an undecomposed peat sample with a total N content of 0 mass-%. This allowed us to predict the specific heat capacity of a peat sample from its MIRS by using the spectral prediction model for peat N content to predict the N content for the peat sample and inserting this into equations (S3) together with the (known) peat temperature.

Plots of measured and predicted c_p versus N content are shown in Fig. S7 and measurements versus fitted values in Fig. S8.

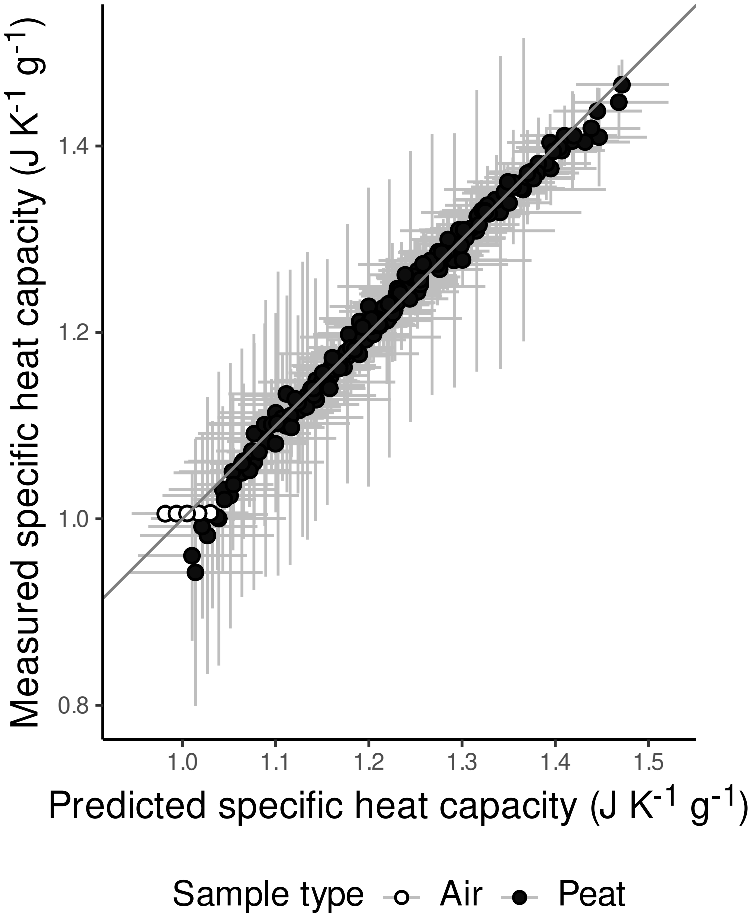

Figure S7: Plot of measured c_p versus predictions by model (S3). Error bars are 95% prediction intervals.

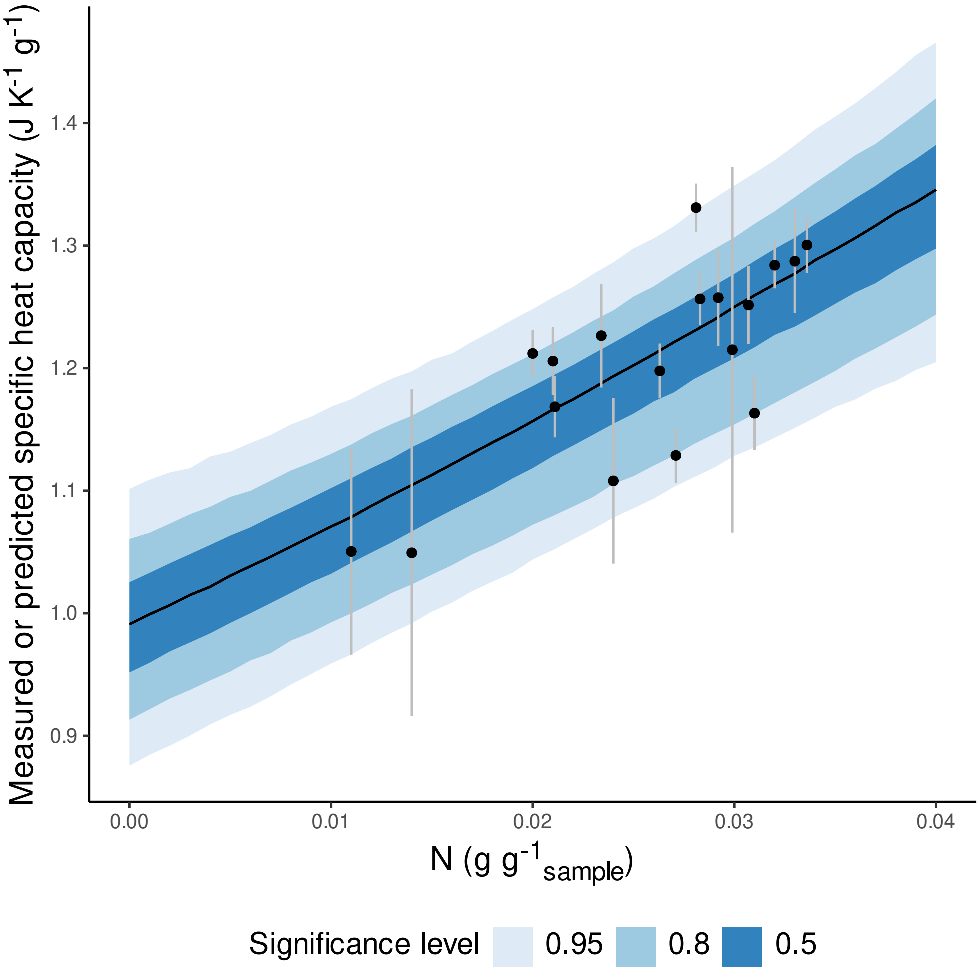

Figure S8: Plot of measured (points) and predicted (lines and shaded areas) c_p. Shaded areas are prediction intervals and error bars represent measurement errors.

S1.4 Dry thermal conductivity ($K_\mathbf{T}$)

The pmird database does not contain measured peat dry thermal conductivity and MIRS measured for the same samples. However, peat dry thermal conductivity can be modeled from peat bulk density (O'Connor et al., 2020).

We therefore modeled the dry thermal conductivity from MIRS by predicting peat bulk density from MIRS and then using the model from O'Connor et al. (2020). We recomputed the model described there with data received from the authors of O'Connor et al. (2020) via email as the data included in the supporting information to O'Connor et al. (2020) were incomplete and some modifications:

$$
\begin{aligned}
K_{\mathrm{T}} \sim &\quad \mathrm{gamma}\left(\phi, \frac{\phi}{\mu_{K_{\mathrm{T}}}}\right) \\
\mu_{K_{\mathrm{T}}} = &\quad \exp(\alpha_{\mu} + \beta_{\mu,1}\rho + \beta_{\mu,2}\log(\rho)) \\
\phi = &\quad \exp(\alpha_{\phi} + \beta_{\phi,1}\rho + \beta_{\phi,2}\log(\rho)),
\end{aligned}
\tag{S4}
$$

where K_{T} is the dry thermal conductivity (W m^{-1} K^{-1}), $\mu_{K_{\mathrm{T}}}$ is the expected dry thermal conductivity (W m^{-1} K^{-1}), α_{μ} is the intercept, $\beta_{\mu,1}$ and $\beta_{\mu,2}$ are the slopes of the relation with ρ and $\log(\rho)$, and ρ is the bulk density (g cm^{-3}). The shape parameter of the gamma distribution, ϕ, was modeled with a similar model (in dependency of bulk density) since the prediction standard deviation was less than expected based on a gamma distribution with constant shape parameter. The modifications consider that K_{T} is > 0 W m^{-1} K^{-1}.
This allowed us to predict the dry thermal conductivity of a peat sample from its MIRS by using the spectral prediction model for peat bulk density to predict the bulk density for the peat sample and inserting this into equation (S4). Plots of measured and predicted K_{T} versus bulk density are shown in Fig. S9 and measurements versus fitted values in Fig. S10.

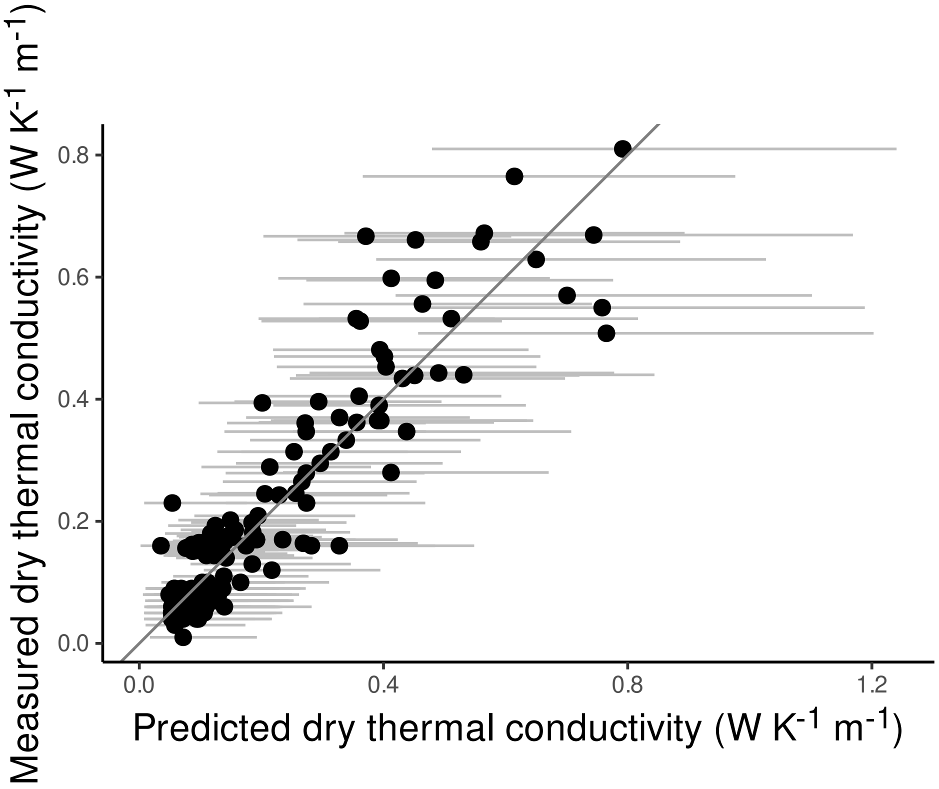

Figure S9: Plot of measured K_{T} versus predictions by model (S4). Error bars are 95% prediction intervals.

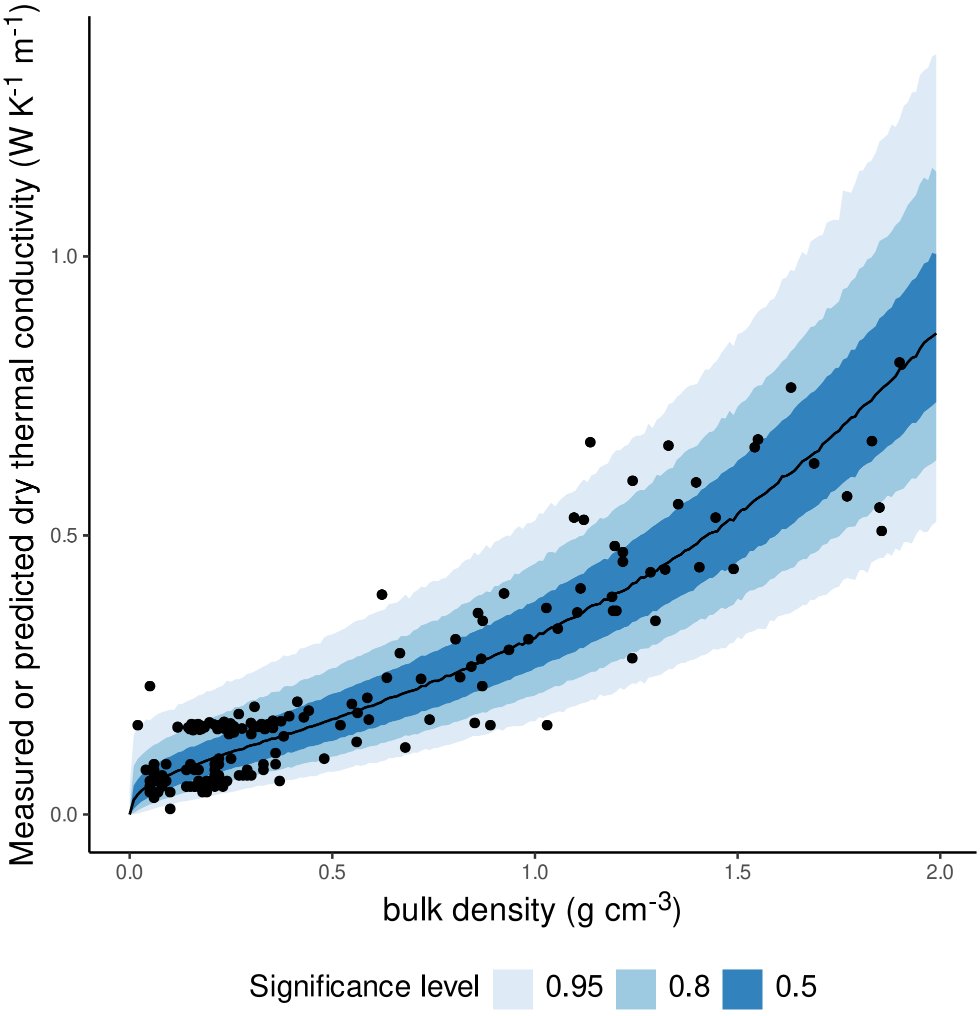

Figure S10: Plot of measured (points) and predicted (lines and shaded areas) K_T. Shaded areas are prediction intervals.

S2 Estimating the standard Gibbs free energy of formation (ΔG_f^0) from elemental contents

S2.1 Modeling approach

The pmird database does not contain ΔG_f^0 values. However, several procedures have been proposed to compute ΔG_f^0 of organic matter (mixtures) with unknown molecular formula from its stoichiometry (see e.g., Popovic, 2019). Such an approach can be applied to peat samples from the pmird database with measured C, H, O, N contents to estimate ΔG_f^0. To this end, we here combine the approaches suggested in Thornton (1917), Patel and Erickson (1981), and Battley (1999) to compute ΔG_f^0, as explained in detail in Popovic (2019).

The standard Gibbs free energy of a sample ($\Delta G_{f,sample}^0$) can be computed from the enthalpy of formation and the entropy of formation, using the Gibbs equation (Battley, 1999; Popovic, 2019):

$$\Delta \mathrm{G}^0_{\mathrm{f,sample}} = \Delta \mathrm{H}^0_{\mathrm{f,sample}} - \mathrm{T}\Delta \mathrm{S}^0_{\mathrm{f,sample}}, \tag{S5}$$

where $\mathrm{T} = 298.15$ K is the temperature under standard conditions, $\Delta \mathrm{H}^0_{\mathrm{f,sample}}$ the standard enthalpy of formation of the peat sample (kJ $\mathrm{mol}_{\mathrm{C}}^{-1}$), and $\Delta \mathrm{S}^0_{\mathrm{f,sample}}$ the standard entropy of formation of the peat sample (J $\mathrm{mol}_{\mathrm{C}}^{-1}$ K^{-1}). The equation is also valid for values normalized to the molar C content (which is a premise in case of peat because we do not know the individual molecular formulas).

$\Delta \mathrm{H}^0_{\mathrm{f,sample}}$ and $\Delta \mathrm{S}^0_{\mathrm{f,sample}}$ can both be derived from the stoichiometry of peat samples (Thornton, 1917; Patel and Erickson, 1981; Battley, 1999; Popovic, 2019), as explained in the two next subsections and described by Popovic (2019). In a third subsection, we describe how uncertainties in estimated $\Delta \mathrm{H}^0_{\mathrm{f,sample}}$ and $\Delta \mathrm{S}^0_{\mathrm{f,sample}}$ are propagated to estimated $\Delta \mathrm{G}^0_{\mathrm{f}}$.

We could check this approach with a subset from the OBIGT database (Helgeson, 1978; Wagman et al., 1982; Shock, 1993; Dale et al., 1997; Richard and Helgeson, 1998; Helgeson et al., 1998; Richard, 2001; LaRowe and Helgeson, 2006a,b; Helgeson et al., 2009; LaRowe and Dick, 2012) from the 'CHNOSZ' R package (version 2.1.0) (Dick, 2019). The OBIGT database is one of the largest open access databases on thermodynamic data (Dick, 2019). To this end, we used the approach described here to estimate $\Delta \mathrm{G}^0_{\mathrm{f}}$ for samples in the OBIGT database and plot $\Delta \mathrm{G}^0_{\mathrm{f}}$ values stored in the OBIGT database for the same compounds and derived by different methods against these estimates. The values were in relative good agreement (supporting Fig. S15).

According to Hess' law, $\Delta \mathrm{H}^0_{\mathrm{f,sample}}$ can be computed from the standard enthalpy of combustion ($\Delta \mathrm{H}^0_{\mathrm{c,sample}}$) and the standard enthalpies of formation of the chemical elements the sample is composed of (Popovic, 2019):

$$\Delta \mathrm{H}^0_{\mathrm{f,sample}} = n_{\mathrm{C}} \mathrm{H}^0_{\mathrm{f,CO_2}} + \frac{1}{2} n_{\mathrm{H}} \Delta \mathrm{H}^0_{\mathrm{f,H_2O}} + \frac{1}{4} n_{\mathrm{P}} \mathrm{H}^0_{\mathrm{f,P_4O_{10}}} + \frac{1}{2} n_{\mathrm{S}} \mathrm{H}^0_{\mathrm{f,SO_2}} - \mathrm{H}^0_{\mathrm{c,sample}}, \tag{S6}$$

where all terms have unit kJ $\mathrm{mol}_{\mathrm{C}}^{-1}$, $\Delta \mathrm{H}^0_{\mathrm{c,sample}}$ is the standard enthalpy of formation for the sample, $\mathrm{H}^0_{\mathrm{c,sample}}$ the standard enthalpy of combustion, n_i the mols of chemical element i per moles of C in the sample (mol_i $\mathrm{mol}_{\mathrm{C}}^{-1}$), and all other terms the standard enthalpies of formation of the subscripted species.

All quantities in equation (S6) can be derived from literature values (we used values derived from the OBIGT database and, for P_4O_{10}, data from (https://webbook.nist.gov/cgi/cbook.cgi?ID=C16752606&Mask=6F) (Linstrom, 1997)), except for $\Delta \mathrm{H}^0_{c,\mathrm{sample}}$, which can be computed with Thornton's rule (Thornton, 1917; Patel and Erickson, 1981; Popovic, 2019):

$$\Delta \mathrm{H}^0_{\mathrm{c,sample}} = \alpha_1 E, \tag{S7}$$

where α_1 is a proportionality constant (kJ $\mathrm{mol}_{\mathrm{C}}^{-1}$) and E the amount of electrons transferred during combustion of an amount of the sample containing 1 mol of C ($\mathrm{mol}_{\mathrm{e^-}}$ $\mathrm{mol}_{\mathrm{C}}^{-1}$). Praameter α_1 can be estimated by regressing measured combustion enthalpies of samples against their

E (see below). Values for E can be computed from known element compositions (assuming formation of SO_2) (Popovic, 2019):

$$E = 4n_{\mathrm{C}} + n_{\mathrm{H}} + 2n_{\mathrm{O}} + 0n_{\mathrm{N}} + 5n_{\mathrm{P}} + 4n_{\mathrm{S}}, \tag{S8}$$

where E is the amount of electrons transferred to oxygen during combustion of an amount of the sample containing one mol of C ($\mathrm{mol}_{\mathrm{e}^-}\ \mathrm{mol}_{\mathrm{C}}^{-1}$) and n_i are the amounts of chemical element i in the same amount of sample sample ($\mathrm{mol}_i\ \mathrm{mol}_{\mathrm{C}}^{-1}$).

S2.2 Model for the enthalpy of combustion ($\Delta \mathrm{H}_{\mathrm{c}}^0$)

The proportionality constant α_1 from equation (S7) has been estimated — using different datasets — to range between -108.99 kJ $\mathrm{mol}_{\mathrm{C}}^{-1}$ and -111.14 kJ $\mathrm{mol}_{\mathrm{C}}^{-1}$ (Battley, 1999). Unfortunately, errors for this estimate, as well as raw data to recompute the models are not straightforwardly accessible and usable from the original studies.

Even though equation (S7) had a good fit to multiple datasets (Thornton, 1917; Patel and Erickson, 1981), peat samples typically cover only a very small range of transferred electrons (E) and therefore, despite a good fit across a large range of E, prediction errors for individual samples can be large in comparison to the range in predicted average values for peat samples. For this reason, we re-computed the model to predict $\Delta \mathrm{H}_{\mathrm{c}}^0$ from E with raw data from the OBIGT database (Helgeson, 1978; Wagman et al., 1982; Shock, 1993; Dale et al., 1997; Richard and Helgeson, 1998; Helgeson et al., 1998; Richard, 2001; LaRowe and Helgeson, 2006a,b; Helgeson et al., 2009; LaRowe and Dick, 2012; Dick, 2019).

$\Delta \mathrm{H}_{\mathrm{c}}^0$ cannot be > 0 because combustion always releases energy. The original model formulations implicitly assume a normal distribution. We suggest an alternative model, where $|\Delta \mathrm{H}_{\mathrm{c}}^0|$ (the absolute value for $\Delta \mathrm{H}_{\mathrm{c}}^0$) is modeled with a gamma distribution. The full model is:

$$\begin{aligned} |\Delta \mathrm{H}_{\mathrm{c,sample}}^0| &\sim \mathrm{gamma}(\mu, \phi) \\ \mu &= \exp(\alpha_1 + \beta \log(E)), \end{aligned} \tag{S9}$$

where gamma(μ, ϕ) is a gamma distribution parameterized with an average value (μ) and a precision parameter (ϕ). Parameter μ is modeled with a log-link function and is assumed to be proportional to $\log(E)$.

For the computations, we used a subset of the OBIGT database (Helgeson, 1978; Wagman et al., 1982; Shock, 1993; Dale et al., 1997; Richard and Helgeson, 1998; Helgeson et al., 1998; Richard, 2001; LaRowe and Helgeson, 2006a,b; Helgeson et al., 2009; LaRowe and Dick, 2012) in the CHNOSZ package (version 2.1.0) (Dick, 2019). The OBIGT database currently is one of the largest open access database on thermodynamic data from which thermodynamic data can directly be retrieved (Dick, 2019).

We subsetted data on organic compounds, CO_2, and CH_4, in either solid, liquid, or gaseous state, for which values for the enthalpy of formation are reported, which consist only of C, H, N, O, S, P, and are reported as simple chemical formulas. This resulted in thermodynamic data for 966 compounds. The majority of thermodynamic data in this subset is derived either from measured (and recalculated) data or using different group additivity algorithms (Richard and Helgeson, 1998; Helgeson et al., 1998; Richard, 2001; LaRowe and Helgeson, 2006a).

Standard combustion enthalpies can be computed from standard formation enthalpies included 275 in the database by Hess' law using the CHNOSZ package (Dick, 2019). The assumed combustion reaction is (Popovic, 2019):

$$C_aH_bO_cN_dP_eS_f + (a + \frac{1}{4}b + \frac{5}{4}e + f)\,O_2\,(g) \longrightarrow aCO_2\,(g) + \frac{b}{2}H_2O\,(l) + \frac{d}{2}N_2\,(g) + \frac{e}{4}P_4O_{10}\,(s) + fSO_2\,(g)$$

The results are shown in Fig. S11 and S12. Our estimated slope is approximately (approxi- 280 mately because of the log-link of the model), -103.7 (-99, -108.5) kJ mol_C^{-1} (average and 95% confidence interval, Fig. S11) (Patel and Erickson, 1981; Battley, 1999; Popovic, 2019) within the lower range of reported values (-108.99 kJ mol_C^{-1} to -111.14 kJ mol_C^{-1} (Battley, 1999)).

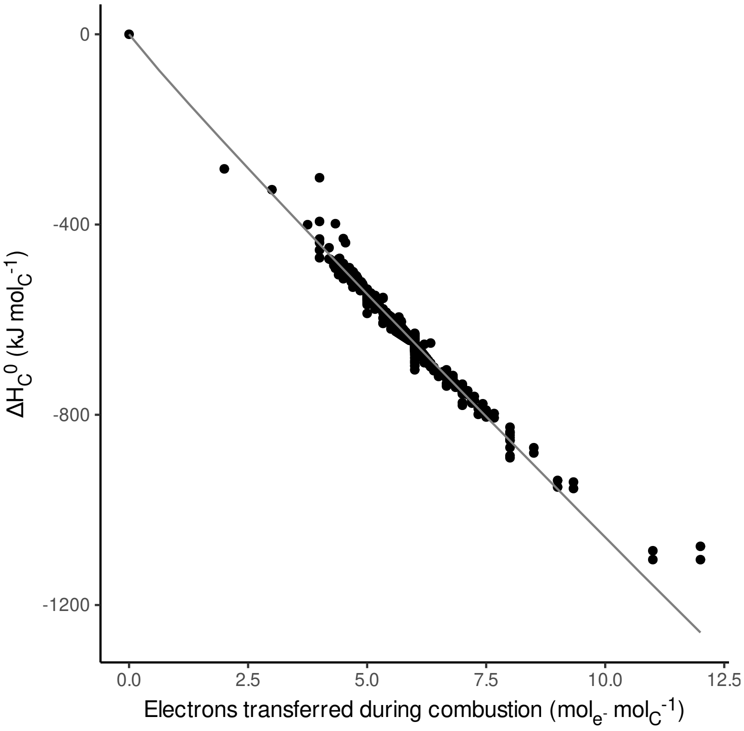

Figure S11: Plot of ΔH_c^0 values in the OBIGT database versus electrons transferred during combustion calculated from equation (S8). The line represents average predictions by model (S9).

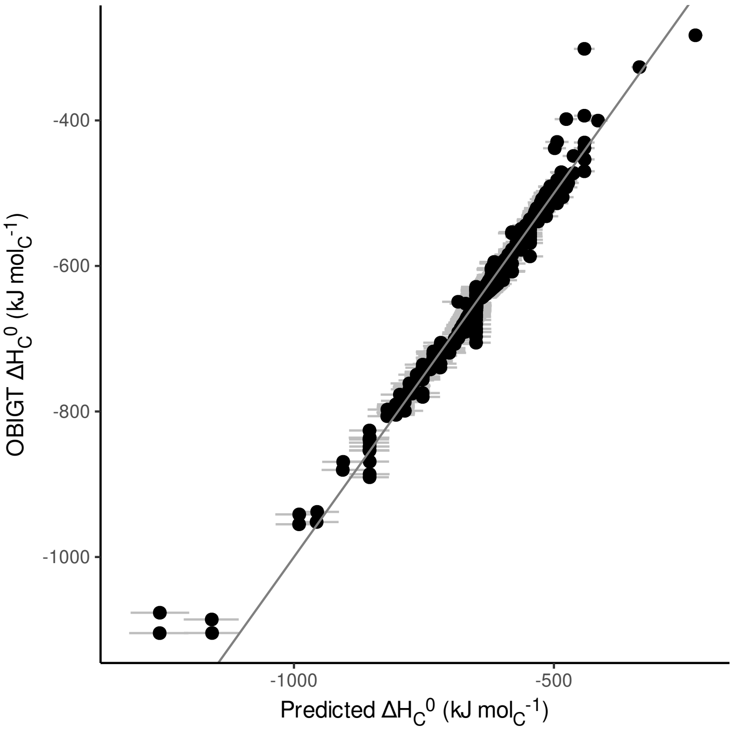

Figure S12: Plot of ΔH_c^0 values in the OBIGT database versus predictions by model (S9).

S2.3 Model for the entropy of formation (ΔS_f^0)

Here, we describe how we recomputed the original model proposed in Battley (1999) that predicts the entropy of formation from sample stoichiometry with data from the OBIGT database (Helgeson, 1978; Wagman et al., 1982; Shock, 1993; Dale et al., 1997; Richard and Helgeson, 1998; Helgeson et al., 1998; Richard, 2001; LaRowe and Helgeson, 2006a,b; Helgeson et al., 2009; LaRowe and Dick, 2012; Dick, 2019) and data from Battley (1999). Similar to ΔH_c^0, we used modified the original model by assuming a gamma distribution with log link function for $|\Delta S_{f,sample}^0|$, since $\Delta S_{f,sample}^0$ is < 0 for all considered compounds/samples:

$$
\begin{aligned}
|\Delta S_{f,sample}^0| &\sim \text{Gamma}(\mu, \phi) \\
\mu &= \exp\left(\alpha_2 + \beta \log\left(\sum_i \frac{S_i^0}{a_i} n_i\right)\right), \qquad \text{(S10)}
\end{aligned}
$$

As data, we used data from Tab. 1 in Battley (1999) extracted with the tabulizer package (Leeper, 2018), and data for compounds from the OBIGT database in their solid state (where $\Delta S_{f,sample}^0$ was computed from standard entropies included in the database and standard entropies from Battley (1999), as described in Battley (1999)) (in total 264 samples). Results are shown in Fig. S13 and S14.

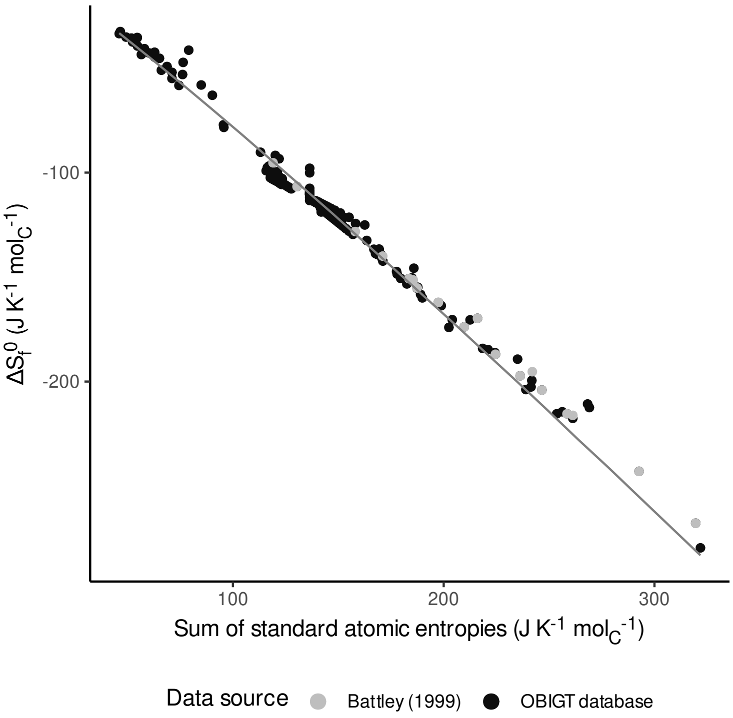

Figure S13: Plot of ΔS_f^0 values in the OBIGT database and from Tab. 1 in Battley (1999) versus the sum of standard atomic entropies calculated from the stoichiometry of the compounds and tabulated standard entropies of atoms ($\sum_i \frac{S_i^0}{a_i} n_i$ in equation (S10)). The line represents average predictions by model (S10).

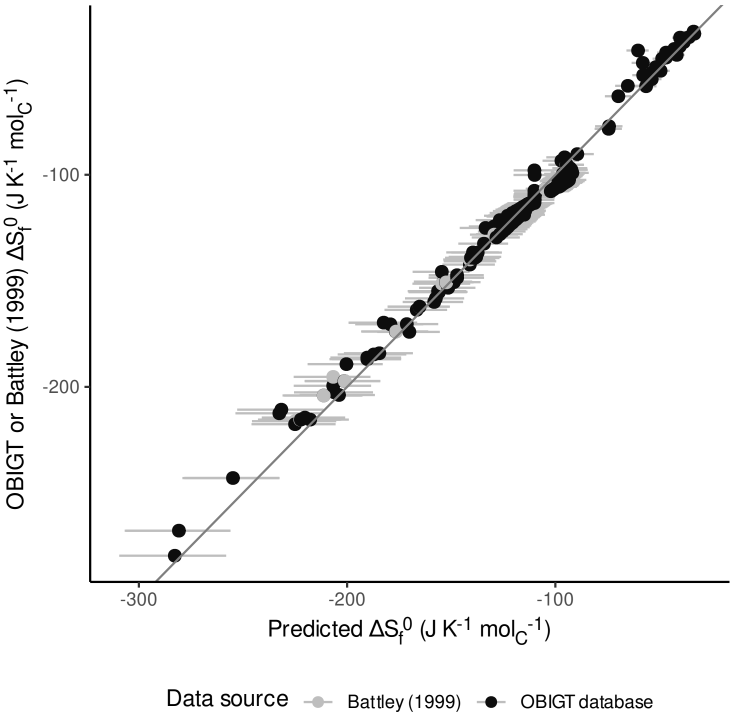

Figure S14: Plot of ΔS_f^0 values in the OBIGT database and from Battley (1999) versus predictions by model (S10). Error bars are 95% prediction intervals.

S2.4 Standard Gibbs free energy of formation (ΔG_f^0)

With the models for the enthalpy of combustion and entropy of formation, we could estimate ΔG_f^0 as described above (subsection S2.1) for peat samples from the pmird database with C, H, N, and O contents (contents of additional elements were also considered when measurements were available). Since the average is estimated precisely and the model assumes i.i.d prediction errors, predictions for different samples are independent and could be well approximated with independent normal distributions. For the samples from the OBIGT database, this modeling approach produces estimates that agree reasonably well with ΔG_f^0 estimates in the OBIGT database (Fig. S15).

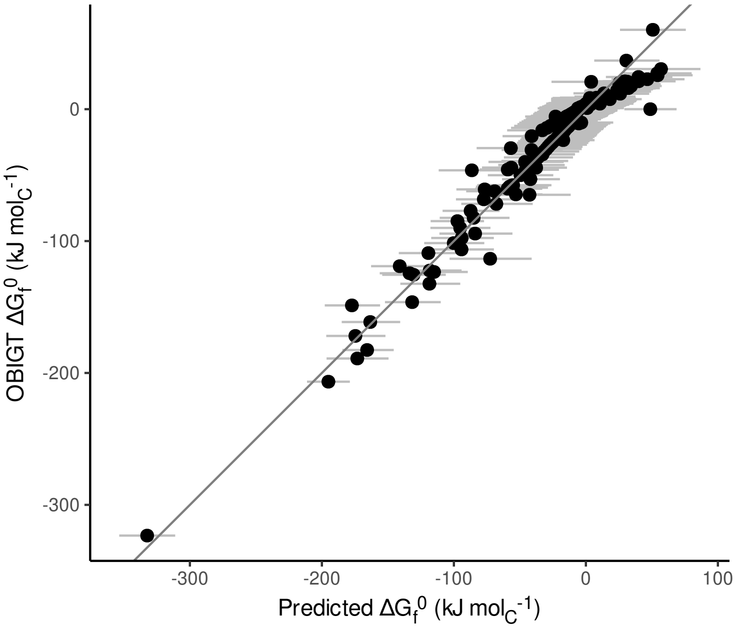

Figure S15: Plot of ΔG_f^0 values in the OBIGT database versus estimates calculated from elemental contents (per mol C). Error bars are 95% prediction intervals.

S3 Metadata for pmird data subsets for each model

Table S1: Summary of the data subset from the pmird database used for each model. "Derivative" indicates what derivative of the spectra were computed. "Samples" gives the number of samples (observations) and, in parentheses, the number of peat cores that were used for each model. "Missing" gives the number of records for which no measurement metadata are available. "Device" lists all measurement devices that were used to record spectra. "Scans" gives the number of single spectra scans that were averaged. "Purge delay" gives the duration during which the measurement cell was purged with synthetic air before measurements (s). "Range" gives, separated by commas, the minimum and maximum of the wavenumber range for the spectra, and the spectral resolution (all in cm^{-1}).

Variable	Derivative	Samples	Missing	Device	Scans	Purge delay	Range
C	0	2382 (141)	480	Bruker Vector 22 FTIR spectrometer, Cary 600 FTIR spectrometer, Cary 660 FTIR spectrometer, Cary 670 FTIR spectrometer, Shimadzu IRTracer-100 spectrophotometer, equipped with a DLaTGS detector, Varian 670 FTIR spectrometer	3 to 200	0 to 180	301 to 600, 4000 to 4500, 0.5 to 1.9

C	1	2382 (141)	480	Bruker Vector 22 FTIR spectrometer, Cary 600 FTIR spectrometer, Cary 660 FTIR spectrometer, Cary 670 FTIR spectrometer, Shimadzu IRTracer-100 spectrophotometer, equipped with a DLaTGS detector, Varian 670 FTIR spectrometer	3 to 200	0 to 180	301 to 600, 4000 to 4500, 0.5 to 1.9
C	2	2382 (141)	480	Bruker Vector 22 FTIR spectrometer, Cary 600 FTIR spectrometer, Cary 660 FTIR spectrometer, Cary 670 FTIR spectrometer, Shimadzu IRTracer-100 spectrophotometer, equipped with a DLaTGS detector, Varian 670 FTIR spectrometer	3 to 200	0 to 180	301 to 600, 4000 to 4500, 0.5 to 1.9
N	0	2376 (141)	474	Bruker Vector 22 FTIR spectrometer, Cary 600 FTIR spectrometer, Cary 660 FTIR spectrometer, Cary 670 FTIR spectrometer, Shimadzu IRTracer-100 spectrophotometer, equipped with a DLaTGS detector, Varian 670 FTIR spectrometer	3 to 200	0 to 180	301 to 600, 4000 to 4500, 0.5 to 1.9
N	1	2376 (141)	474	Bruker Vector 22 FTIR spectrometer, Cary 600 FTIR spectrometer, Cary 660 FTIR spectrometer, Cary 670 FTIR spectrometer, Shimadzu IRTracer-100 spectrophotometer, equipped with a DLaTGS detector, Varian 670 FTIR spectrometer	3 to 200	0 to 180	301 to 600, 4000 to 4500, 0.5 to 1.9
N	2	2376 (141)	474	Bruker Vector 22 FTIR spectrometer, Cary 600 FTIR spectrometer, Cary 660 FTIR spectrometer, Cary 670 FTIR spectrometer, Shimadzu IRTracer-100 spectrophotometer, equipped with a DLaTGS detector, Varian 670 FTIR spectrometer	3 to 200	0 to 180	301 to 600, 4000 to 4500, 0.5 to 1.9
O	0	100 (16)	45	Cary 670 FTIR spectrometer	32	180	600, 4000 to 4002, 0.5 to 1.9
O	1	100 (16)	45	Cary 670 FTIR spectrometer	32	180	600, 4000 to 4002, 0.5 to 1.9

O	2	100 (16)	45	Cary 670 FTIR spectrometer	32	180	600, 4000 to 4002, 0.5 to 1.9
H	0	100 (16)	45	Cary 670 FTIR spectrometer	32	180	600, 4000 to 4002, 0.5 to 1.9
H	1	100 (16)	45	Cary 670 FTIR spectrometer	32	180	600, 4000 to 4002, 0.5 to 1.9
H	2	100 (16)	45	Cary 670 FTIR spectrometer	32	180	600, 4000 to 4002, 0.5 to 1.9
P	0	869 (47)	123	Cary 600 FTIR spectrometer, Cary 660 FTIR spectrometer, Cary 670 FTIR spectrometer, Varian 670 FTIR spectrometer	3 to 64	0 to 180	399 to 600, 4000 to 4002, 0.5 to 1.9
P	1	869 (47)	123	Cary 600 FTIR spectrometer, Cary 660 FTIR spectrometer, Cary 670 FTIR spectrometer, Varian 670 FTIR spectrometer	3 to 64	0 to 180	399 to 600, 4000 to 4002, 0.5 to 1.9
P	2	869 (47)	123	Cary 600 FTIR spectrometer, Cary 660 FTIR spectrometer, Cary 670 FTIR spectrometer, Varian 670 FTIR spectrometer	3 to 64	0 to 180	399 to 600, 4000 to 4002, 0.5 to 1.9
S	0	1485 (104)	294	Bruker Vector 22 FTIR spectrometer, Cary 600 FTIR spectrometer, Cary 660 FTIR spectrometer, Cary 670 FTIR spectrometer, Varian 670 FTIR spectrometer	3 to 64	0 to 180	301 to 600, 4000 to 4500, 0.5 to 1.9
S	1	1485 (104)	294	Bruker Vector 22 FTIR spectrometer, Cary 600 FTIR spectrometer, Cary 660 FTIR spectrometer, Cary 670 FTIR spectrometer, Varian 670 FTIR spectrometer	3 to 64	0 to 180	301 to 600, 4000 to 4500, 0.5 to 1.9
S	2	1485 (104)	294	Bruker Vector 22 FTIR spectrometer, Cary 600 FTIR spectrometer, Cary 660 FTIR spectrometer, Cary 670 FTIR spectrometer, Varian 670 FTIR spectrometer	3 to 64	0 to 180	301 to 600, 4000 to 4500, 0.5 to 1.9
K	0	870 (47)	124	Cary 600 FTIR spectrometer, Cary 660 FTIR spectrometer, Cary 670 FTIR spectrometer, Varian 670 FTIR spectrometer	3 to 64	0 to 180	399 to 600, 4000 to 4002, 0.5 to 1.9
K	1	870 (47)	124	Cary 600 FTIR spectrometer, Cary 660 FTIR spectrometer, Cary 670 FTIR spectrometer, Varian 670 FTIR spectrometer	3 to 64	0 to 180	399 to 600, 4000 to 4002, 0.5 to 1.9

K	2	870 (47)	124	Cary 600 FTIR spectrometer, Cary 660 FTIR spectrometer, Cary 670 FTIR spectrometer, Varian 670 FTIR spectrometer	3 to 64	0 to 180	399 to 600, 4000 to 4002, 0.5 to 1.9
Ti	0	869 (47)	123	Cary 600 FTIR spectrometer, Cary 660 FTIR spectrometer, Cary 670 FTIR spectrometer, Varian 670 FTIR spectrometer	3 to 64	0 to 180	399 to 600, 4000 to 4002, 0.5 to 1.9
Ti	1	869 (47)	123	Cary 600 FTIR spectrometer, Cary 660 FTIR spectrometer, Cary 670 FTIR spectrometer, Varian 670 FTIR spectrometer	3 to 64	0 to 180	399 to 600, 4000 to 4002, 0.5 to 1.9
Ti	2	869 (47)	123	Cary 600 FTIR spectrometer, Cary 660 FTIR spectrometer, Cary 670 FTIR spectrometer, Varian 670 FTIR spectrometer	3 to 64	0 to 180	399 to 600, 4000 to 4002, 0.5 to 1.9
Si	0	866 (47)	123	Cary 600 FTIR spectrometer, Cary 660 FTIR spectrometer, Cary 670 FTIR spectrometer, Varian 670 FTIR spectrometer	3 to 64	0 to 180	399 to 600, 4000 to 4002, 0.5 to 1.9
Si	1	866 (47)	123	Cary 600 FTIR spectrometer, Cary 660 FTIR spectrometer, Cary 670 FTIR spectrometer, Varian 670 FTIR spectrometer	3 to 64	0 to 180	399 to 600, 4000 to 4002, 0.5 to 1.9
Si	2	866 (47)	123	Cary 600 FTIR spectrometer, Cary 660 FTIR spectrometer, Cary 670 FTIR spectrometer, Varian 670 FTIR spectrometer	3 to 64	0 to 180	399 to 600, 4000 to 4002, 0.5 to 1.9
Ca	0	871 (47)	125	Cary 600 FTIR spectrometer, Cary 660 FTIR spectrometer, Cary 670 FTIR spectrometer, Varian 670 FTIR spectrometer	3 to 64	0 to 180	399 to 600, 4000 to 4002, 0.5 to 1.9
Ca	1	871 (47)	125	Cary 600 FTIR spectrometer, Cary 660 FTIR spectrometer, Cary 670 FTIR spectrometer, Varian 670 FTIR spectrometer	3 to 64	0 to 180	399 to 600, 4000 to 4002, 0.5 to 1.9
Ca	2	871 (47)	125	Cary 600 FTIR spectrometer, Cary 660 FTIR spectrometer, Cary 670 FTIR spectrometer, Varian 670 FTIR spectrometer	3 to 64	0 to 180	399 to 600, 4000 to 4002, 0.5 to 1.9

δ^{13}C	0	1241 (48)	128	Bruker Vector 22 FTIR spectrometer, Cary 600 FTIR spectrometer, Cary 660 FTIR spectrometer, Cary 670 FTIR spectrometer	3 to 64	0 to 180	301 to 600, 4000 to 4500, 0.5 to 1.9
δ^{13}C	1	1241 (48)	128	Bruker Vector 22 FTIR spectrometer, Cary 600 FTIR spectrometer, Cary 660 FTIR spectrometer, Cary 670 FTIR spectrometer	3 to 64	0 to 180	301 to 600, 4000 to 4500, 0.5 to 1.9
δ^{13}C	2	1241 (48)	128	Bruker Vector 22 FTIR spectrometer, Cary 600 FTIR spectrometer, Cary 660 FTIR spectrometer, Cary 670 FTIR spectrometer	3 to 64	0 to 180	301 to 600, 4000 to 4500, 0.5 to 1.9
δ^{15}N	0	1241 (48)	128	Bruker Vector 22 FTIR spectrometer, Cary 600 FTIR spectrometer, Cary 660 FTIR spectrometer, Cary 670 FTIR spectrometer	3 to 64	0 to 180	301 to 600, 4000 to 4500, 0.5 to 1.9
δ^{15}N	1	1241 (48)	128	Bruker Vector 22 FTIR spectrometer, Cary 600 FTIR spectrometer, Cary 660 FTIR spectrometer, Cary 670 FTIR spectrometer	3 to 64	0 to 180	301 to 600, 4000 to 4500, 0.5 to 1.9
δ^{15}N	2	1241 (48)	128	Bruker Vector 22 FTIR spectrometer, Cary 600 FTIR spectrometer, Cary 660 FTIR spectrometer, Cary 670 FTIR spectrometer	3 to 64	0 to 180	301 to 600, 4000 to 4500, 0.5 to 1.9
NOSC	0	100 (16)	45	Cary 670 FTIR spectrometer	32	180	600, 4000 to 4002, 0.5 to 1.9
NOSC	1	100 (16)	45	Cary 670 FTIR spectrometer	32	180	600, 4000 to 4002, 0.5 to 1.9
NOSC	2	100 (16)	45	Cary 670 FTIR spectrometer	32	180	600, 4000 to 4002, 0.5 to 1.9
ΔG_f^0	0	100 (16)	45	Cary 670 FTIR spectrometer	32	180	600, 4000 to 4002, 0.5 to 1.9
ΔG_f^0	1	100 (16)	45	Cary 670 FTIR spectrometer	32	180	600, 4000 to 4002, 0.5 to 1.9
ΔG_f^0	2	100 (16)	45	Cary 670 FTIR spectrometer	32	180	600, 4000 to 4002, 0.5 to 1.9
Loss on ignition	0	101 (14)	0	Cary 660 FTIR spectrometer, Cary 670 FTIR spectrometer, Varian 670 FTIR spectrometer	3 to 32	180	399 to 600, 4001 to 4002, 1 to 1.9
Loss on ignition	1	101 (14)	0	Cary 660 FTIR spectrometer, Cary 670 FTIR spectrometer, Varian 670 FTIR spectrometer	3 to 32	180	399 to 600, 4001 to 4002, 1 to 1.9
Loss on ignition	2	101 (14)	0	Cary 660 FTIR spectrometer, Cary 670 FTIR spectrometer, Varian 670 FTIR spectrometer	3 to 32	180	399 to 600, 4001 to 4002, 1 to 1.9

Bulk density	0	889 (56)	323	Bruker Vector 22 FTIR spectrometer, Cary 600 FTIR spectrometer, Cary 660 FTIR spectrometer, Cary 670 FTIR spectrometer, Varian 670 FTIR spectrometer	3 to 64	0 to 180	301 to 600, 4001 to 4500, 1 to 1.9
Bulk density	1	889 (56)	323	Bruker Vector 22 FTIR spectrometer, Cary 600 FTIR spectrometer, Cary 660 FTIR spectrometer, Cary 670 FTIR spectrometer, Varian 670 FTIR spectrometer	3 to 64	0 to 180	301 to 600, 4001 to 4500, 1 to 1.9
Bulk density	2	889 (56)	323	Bruker Vector 22 FTIR spectrometer, Cary 600 FTIR spectrometer, Cary 660 FTIR spectrometer, Cary 670 FTIR spectrometer, Varian 670 FTIR spectrometer	3 to 64	0 to 180	301 to 600, 4001 to 4500, 1 to 1.9
C/N	0	2176 (137)	465	Bruker Vector 22 FTIR spectrometer, Cary 600 FTIR spectrometer, Cary 660 FTIR spectrometer, Cary 670 FTIR spectrometer, Shimadzu IRTracer-100 spectrophotometer, equipped with a DLaTGS detector, Varian 670 FTIR spectrometer	3 to 200	0 to 180	301 to 600, 4000 to 4500, 0.5 to 1.9
C/N	1	2176 (137)	465	Bruker Vector 22 FTIR spectrometer, Cary 600 FTIR spectrometer, Cary 660 FTIR spectrometer, Cary 670 FTIR spectrometer, Shimadzu IRTracer-100 spectrophotometer, equipped with a DLaTGS detector, Varian 670 FTIR spectrometer	3 to 200	0 to 180	301 to 600, 4000 to 4500, 0.5 to 1.9
C/N	2	2176 (137)	465	Bruker Vector 22 FTIR spectrometer, Cary 600 FTIR spectrometer, Cary 660 FTIR spectrometer, Cary 670 FTIR spectrometer, Shimadzu IRTracer-100 spectrophotometer, equipped with a DLaTGS detector, Varian 670 FTIR spectrometer	3 to 200	0 to 180	301 to 600, 4000 to 4500, 0.5 to 1.9
O/C	0	100 (16)	45	Cary 670 FTIR spectrometer	32	180	600, 4000 to 4002, 0.5 to 1.9
O/C	1	100 (16)	45	Cary 670 FTIR spectrometer	32	180	600, 4000 to 4002, 0.5 to 1.9

O/C	2	100 (16)	45	Cary 670 FTIR spectrometer	32	180	600, 4000 to 4002, 0.5 to 1.9
H/C	0	100 (16)	45	Cary 670 FTIR spectrometer	32	180	600, 4000 to 4002, 0.5 to 1.9
H/C	1	100 (16)	45	Cary 670 FTIR spectrometer	32	180	600, 4000 to 4002, 0.5 to 1.9
H/C	2	100 (16)	45	Cary 670 FTIR spectrometer	32	180	600, 4000 to 4002, 0.5 to 1.9

Table S2: Geographical coverage of the peat core data used for each model. "Derivative" indicates what derivative of the spectra were computed. "Map" shows the sampling locations of the peat cores. White filled points indicate peat cores that were not used to train the models, but only for model testing. Source of the land surface geometry: https://www.naturalearthdata.com.

Variable	Derivative	Map
C	0	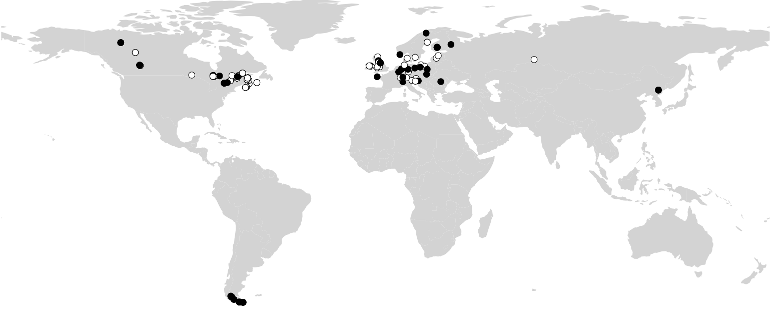
C	1	
C	2	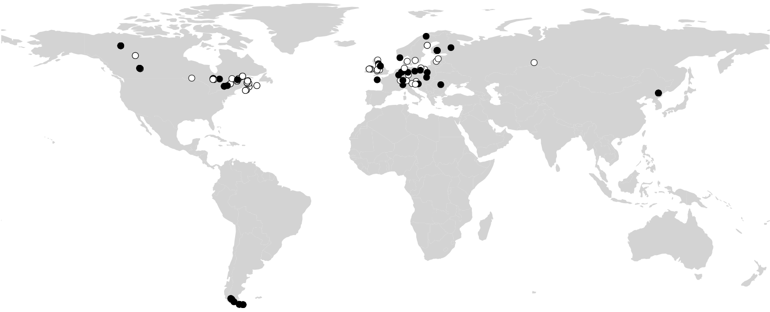

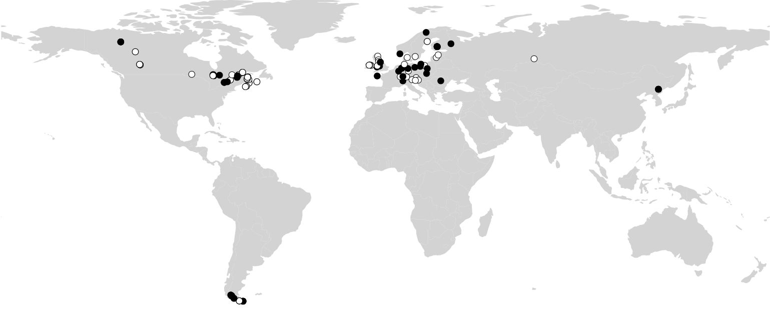

N 0

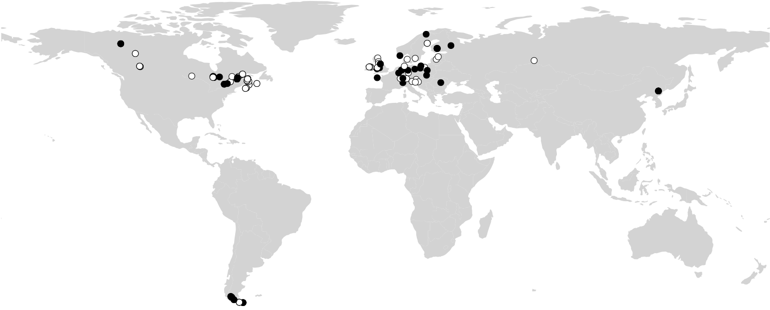

N 1

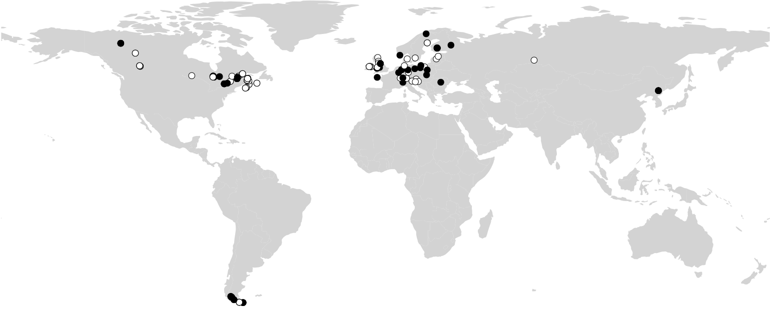

N 2

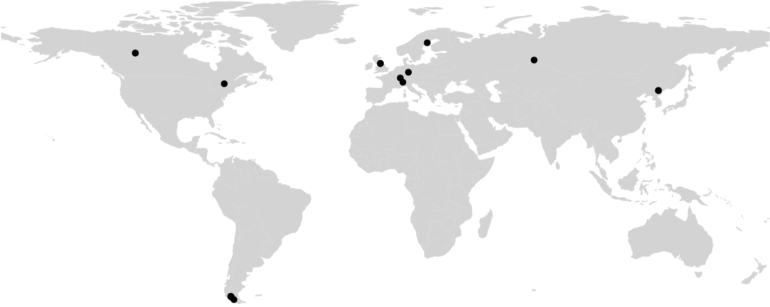

O 0

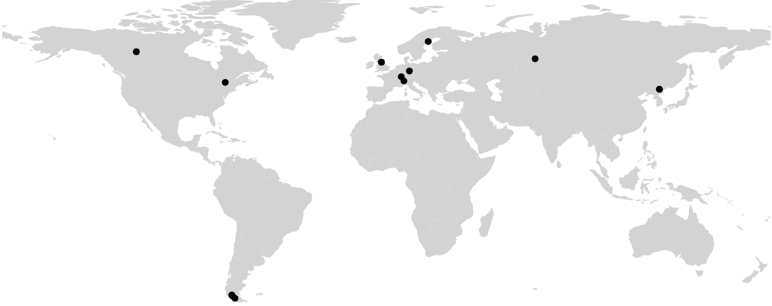

O 1

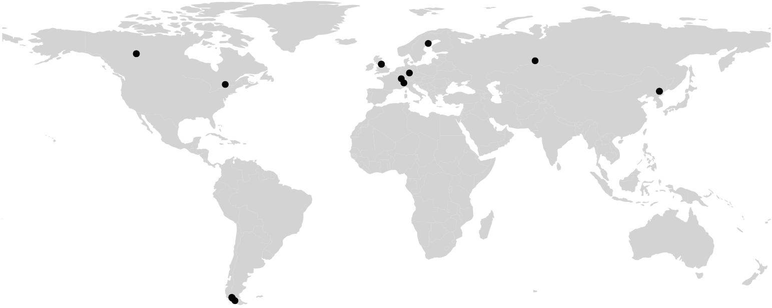

O 2

H 0

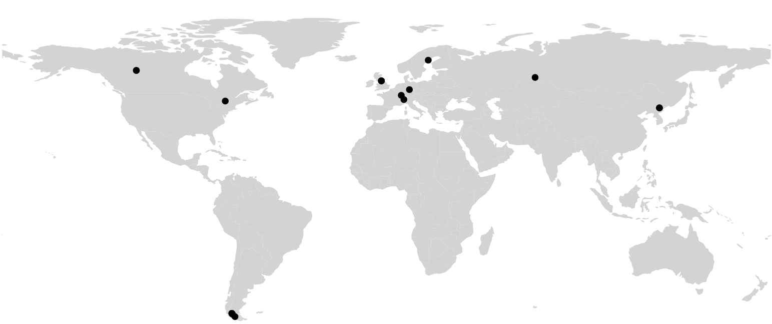

H 1

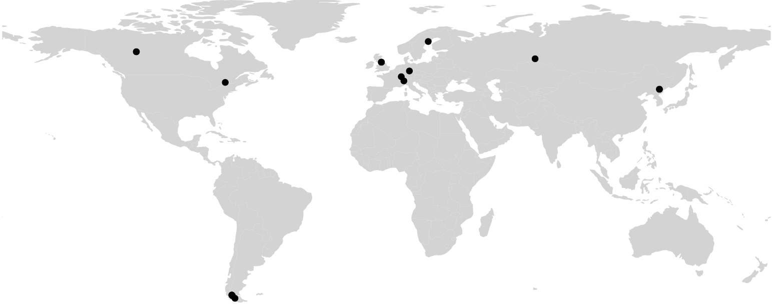

H 2

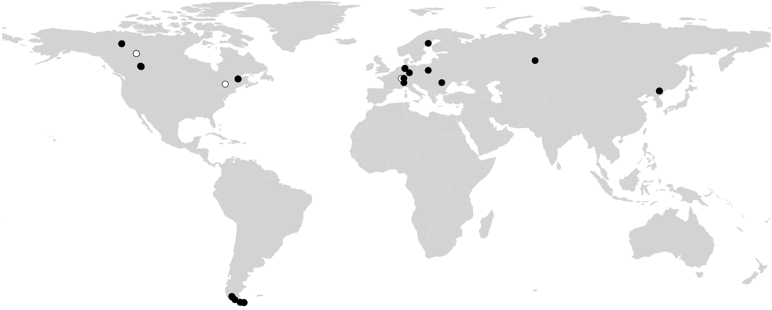

P 0

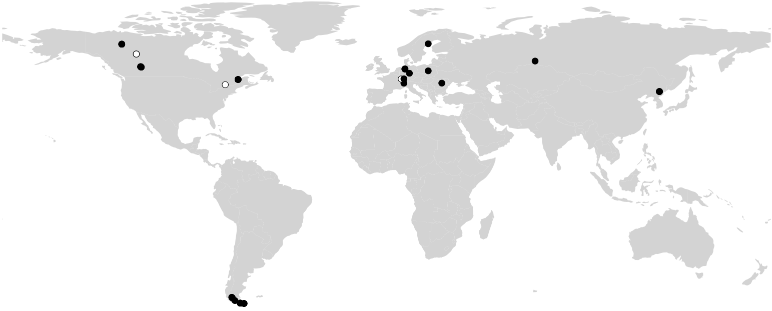

P 1

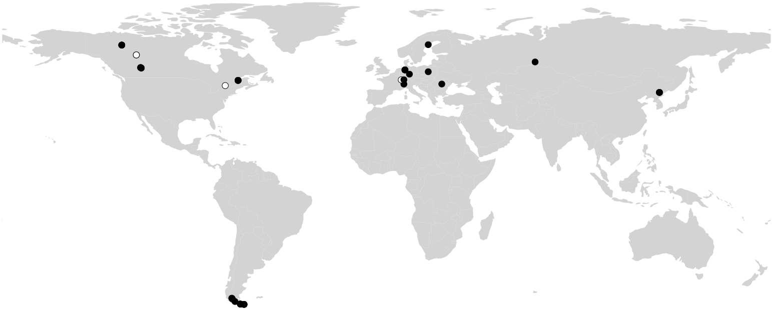

P 2

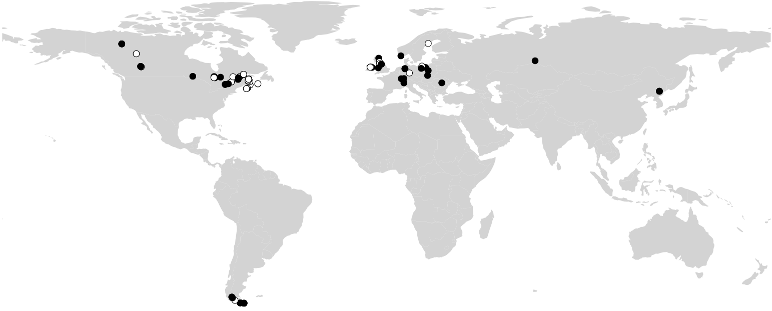

S 0

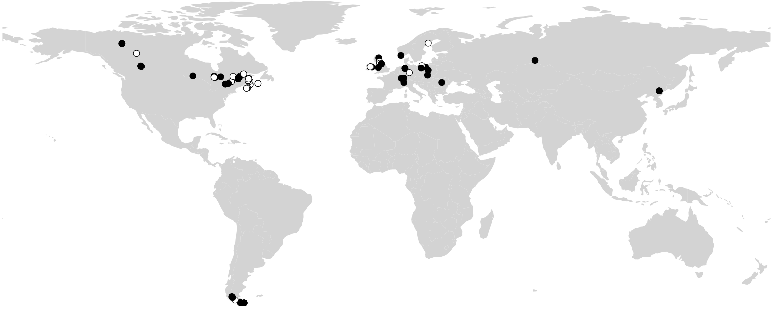

S 1

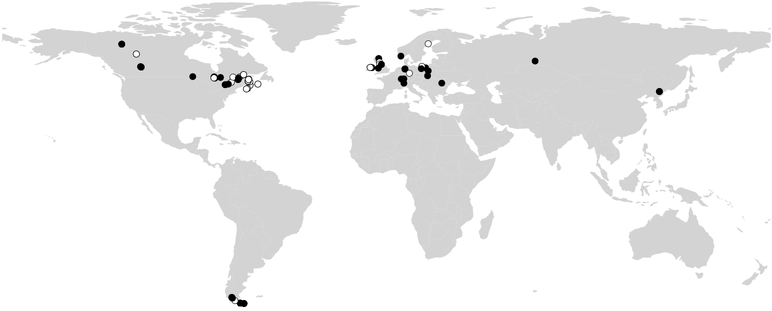

S 2

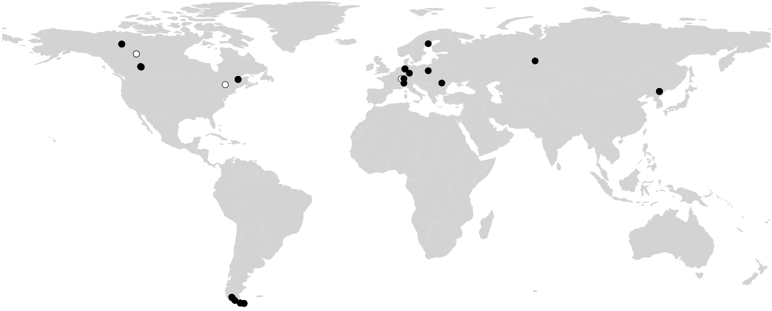

K 0

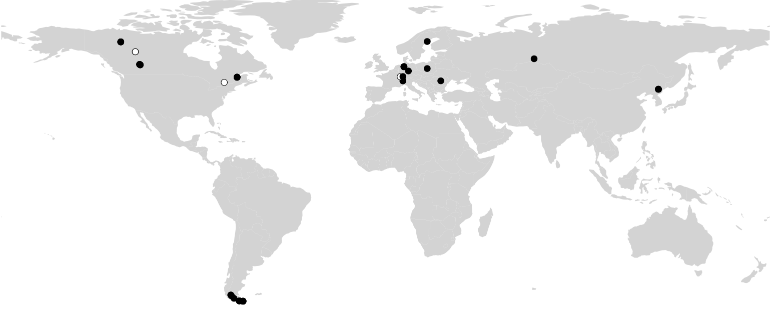

K 1

K 2

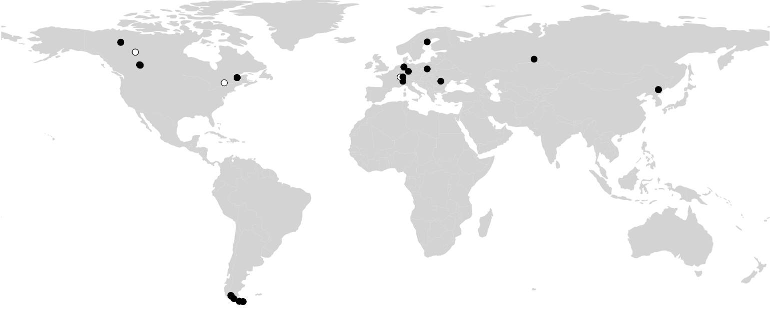

Ti 0

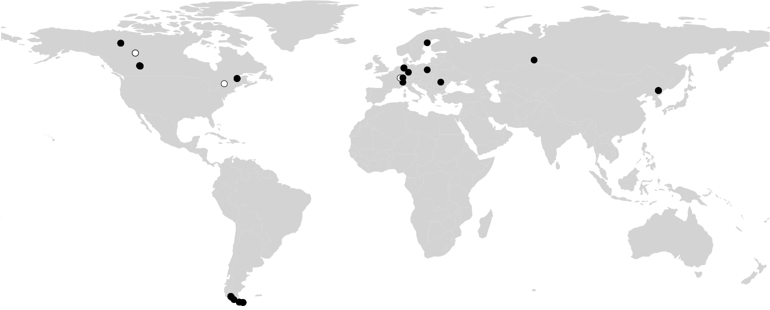

Ti 1

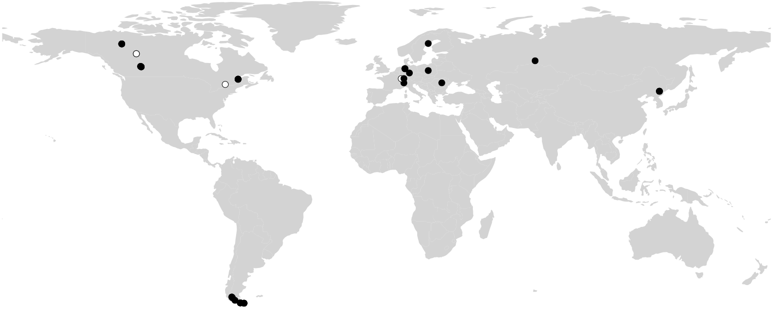

Ti 2

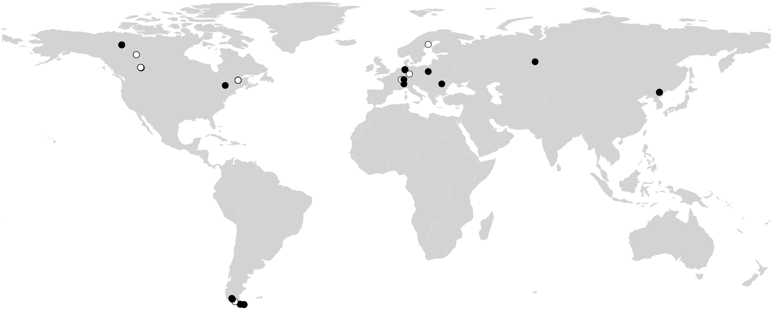

Si 0

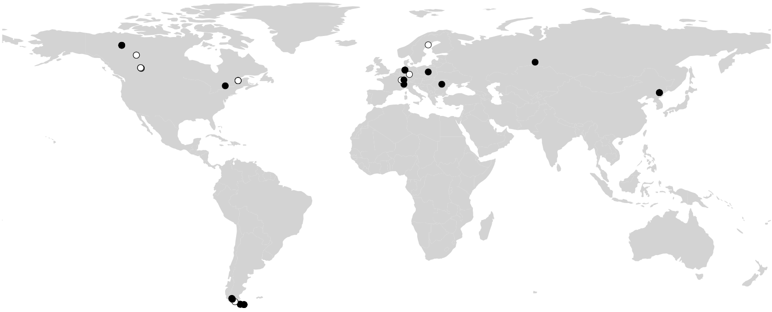

Si 1

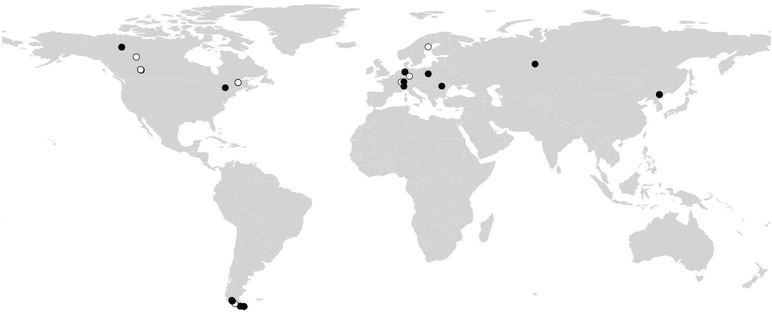

Si 2

Ca 0

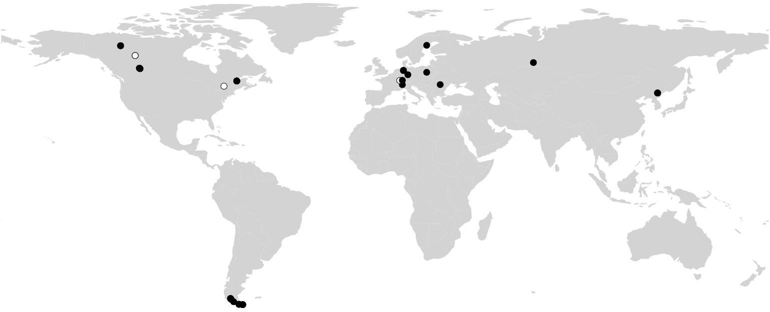

Ca 1

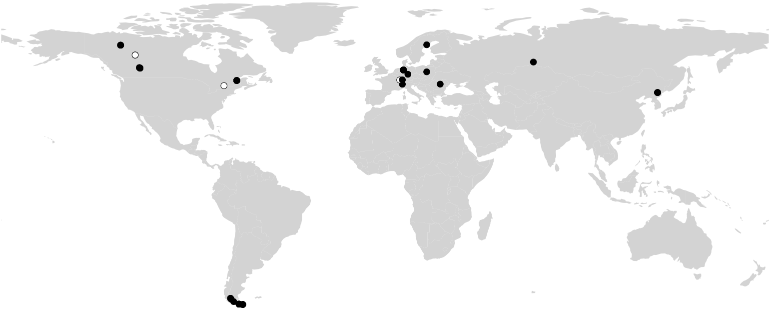

Ca 2

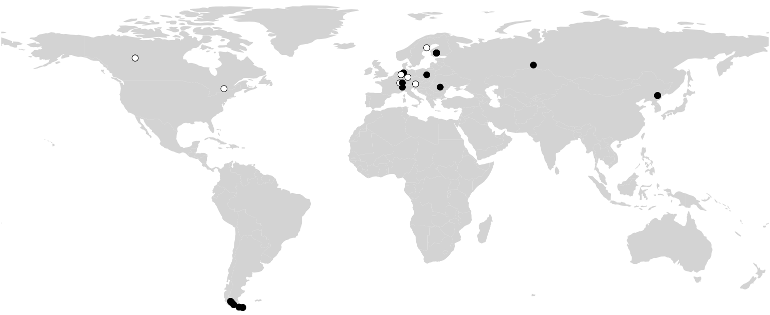

δ^{13}C 0

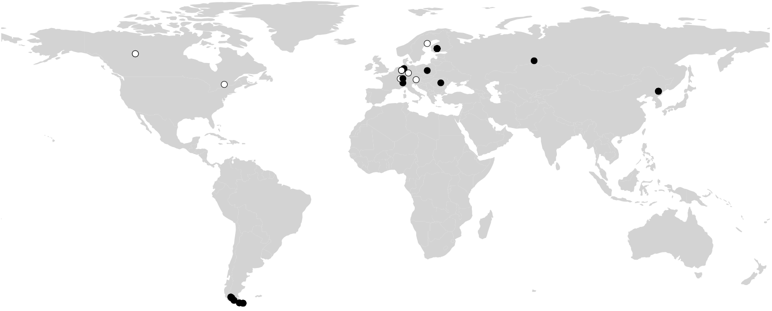

δ^{13}C 1

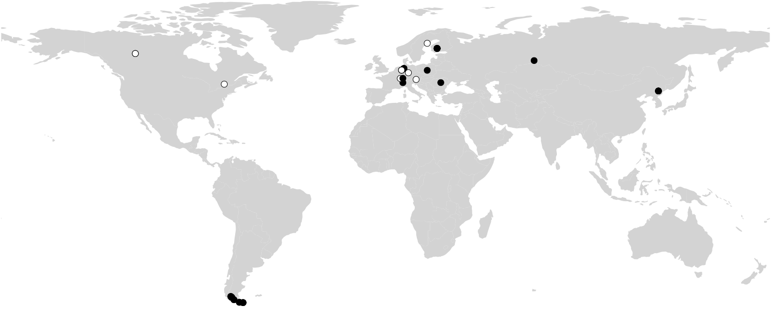

δ^{13}C 2

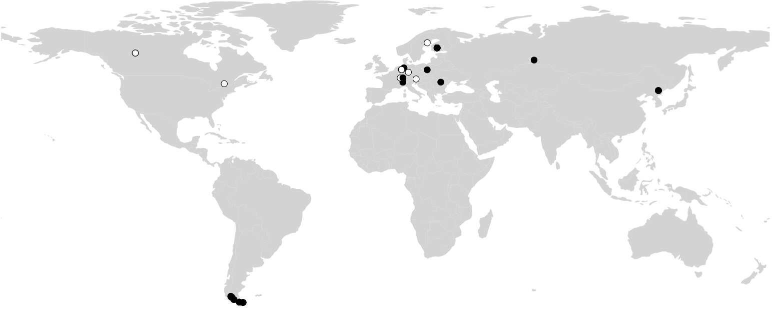

δ^{15}N 0

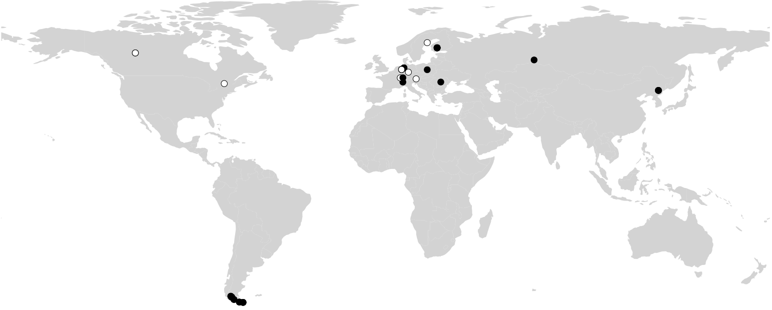

δ^{15}N 1

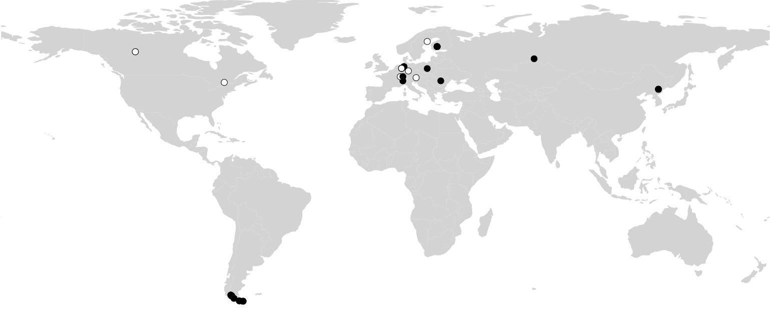

δ^{15}N 2

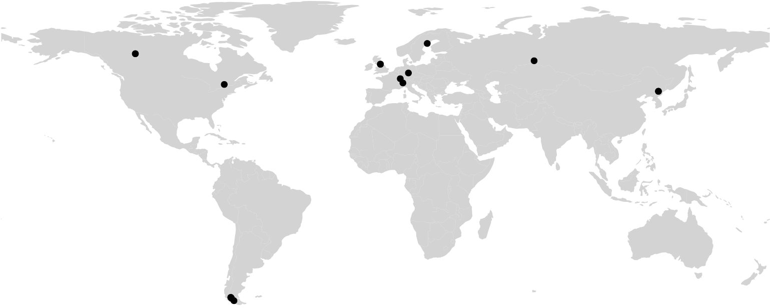

NOSC 0

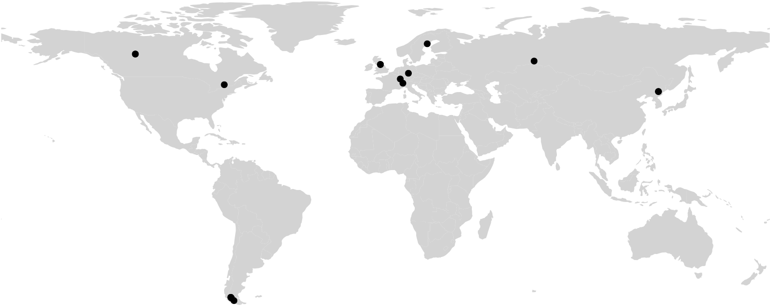

NOSC 1

NOSC 2

ΔG_f^0 0

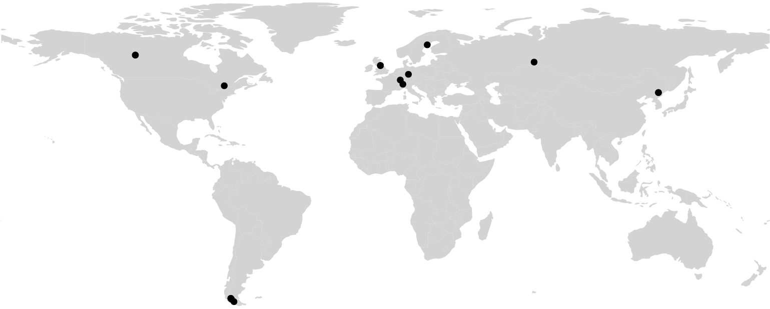

ΔG_f^0 1

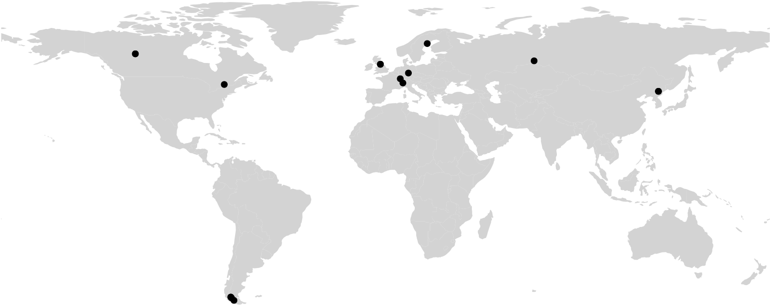

ΔG_f^0 2

Loss on ignition 0

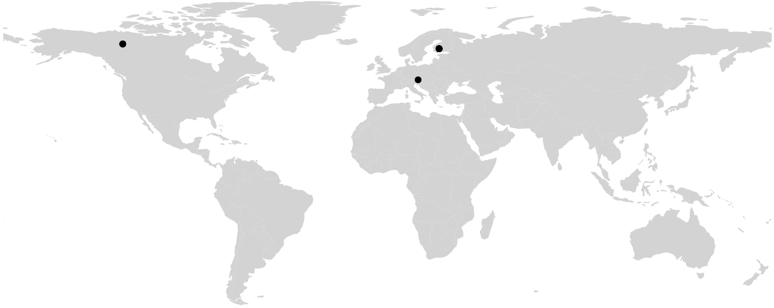

Loss on ignition 1

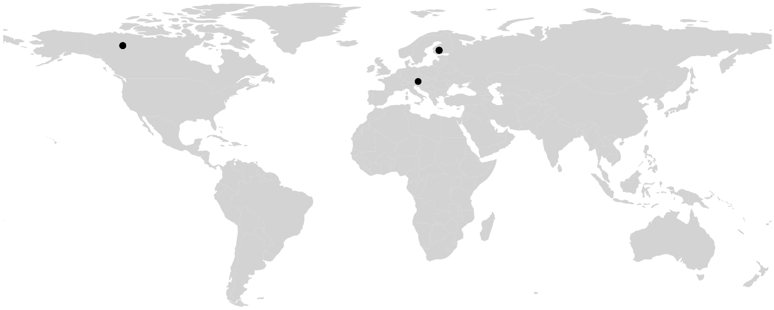

Loss on ignition 2

Bulk density 0

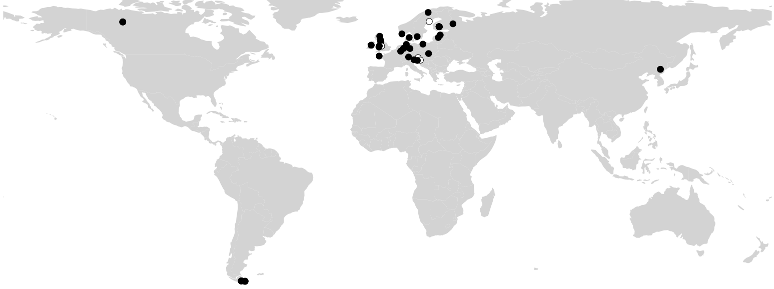

Bulk density 1

Bulk density 2

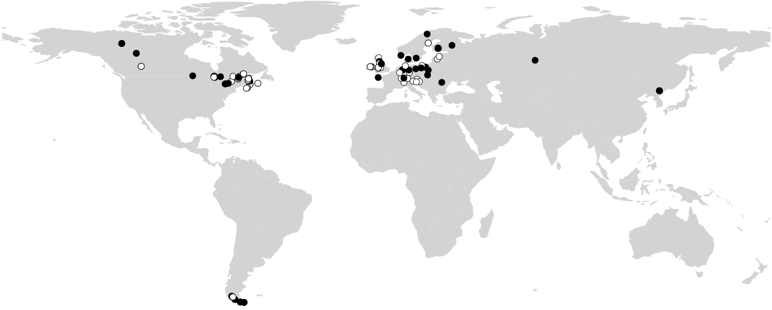

C/N 0

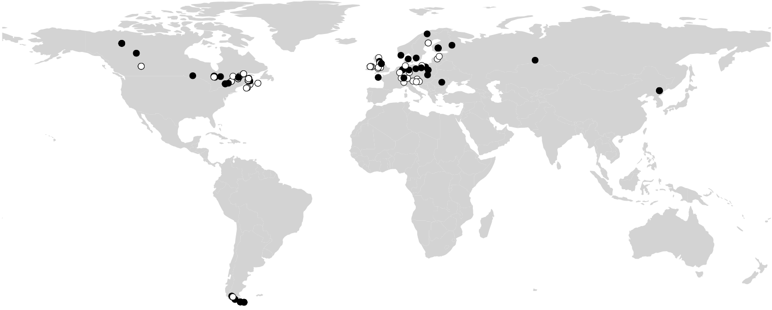

C/N 1

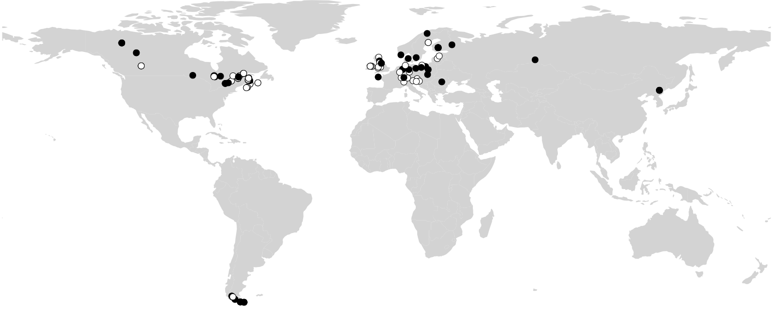

C/N 2

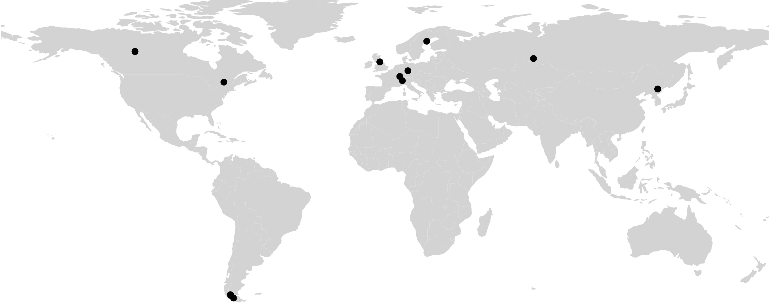

O/C 0

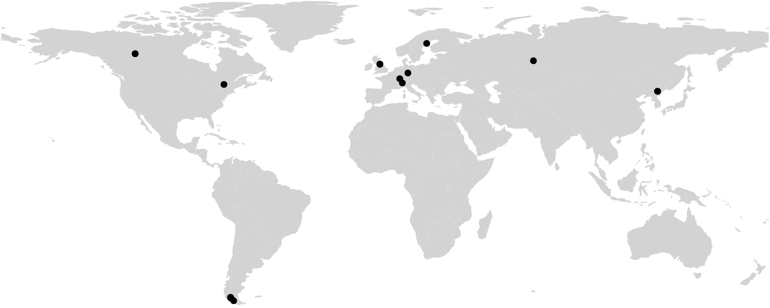

O/C 1

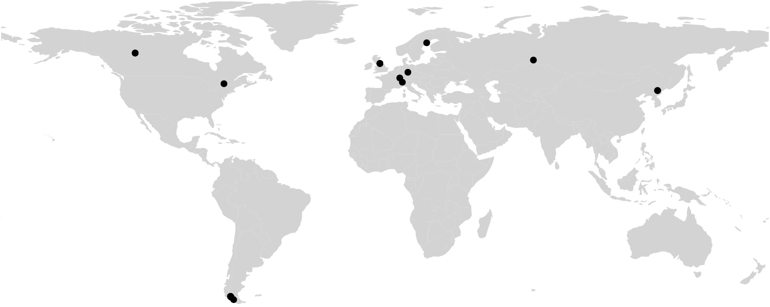

O/C 2

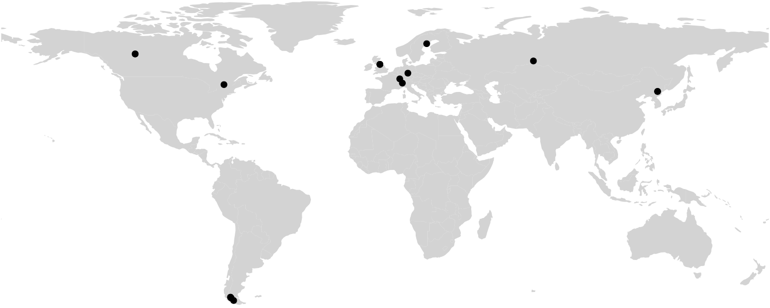

H/C 0

H/C	1	
H/C	2	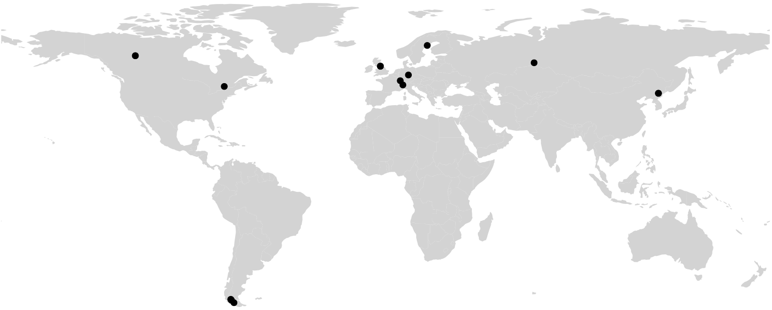

S4 Model evaluation

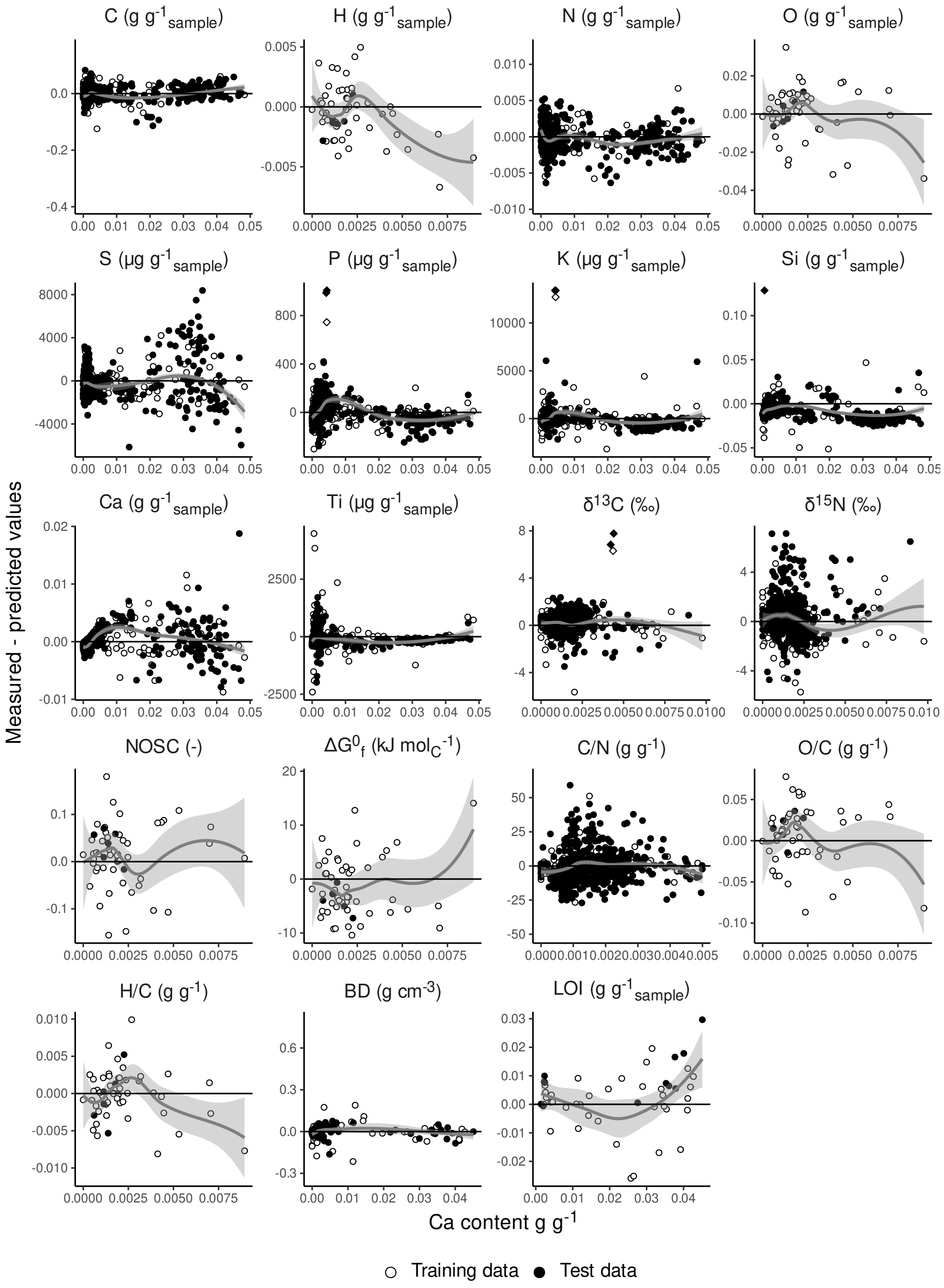

Figure S16: Measured minus predicted values (by the best model) for all target variables versus measured Ca contents (predictions for samples without Ca measurements are not shown). Lines and shaded areas are LOESS smoothers and 95% confidence intervals.

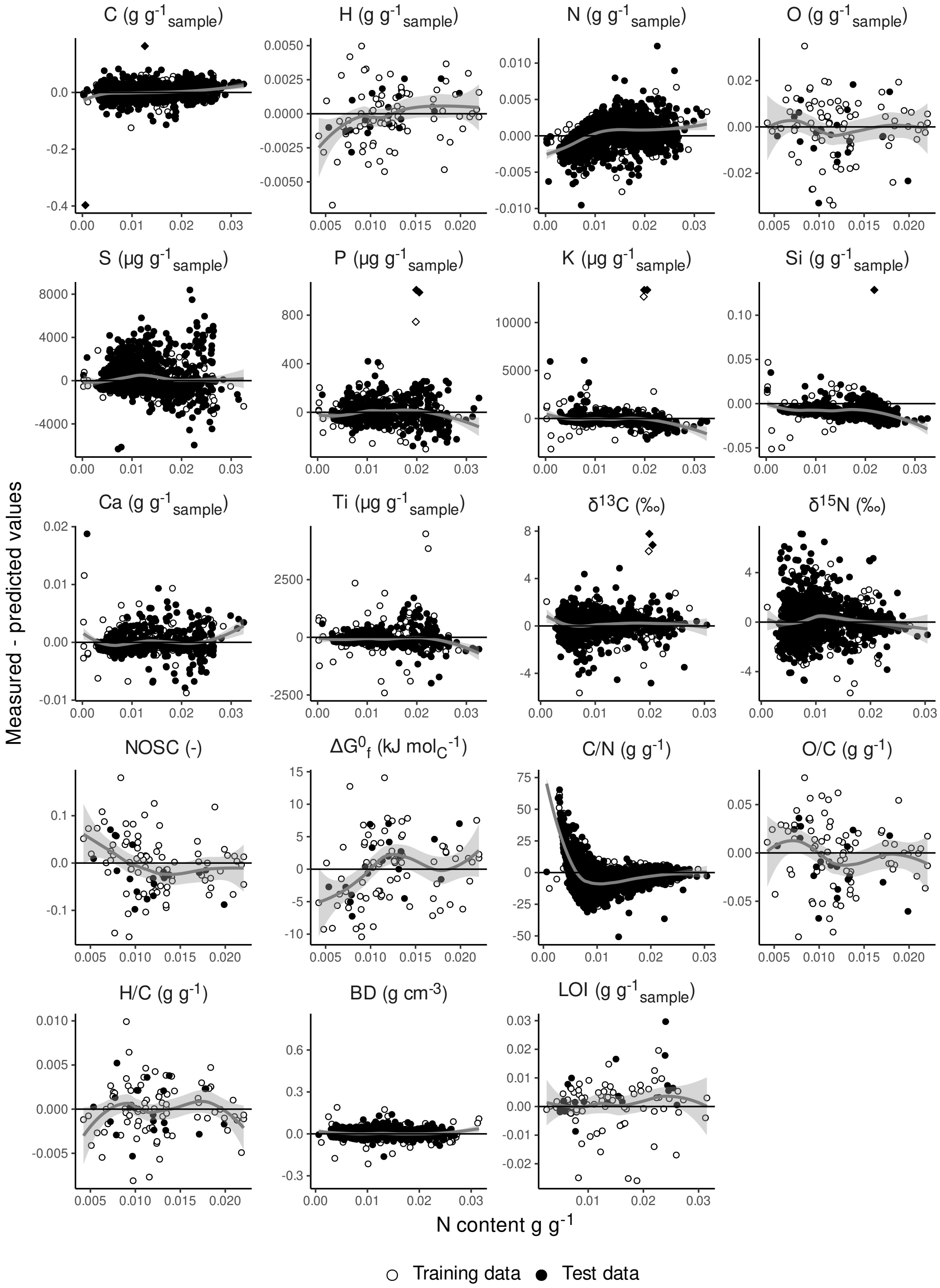

Figure S17: Measured minus predicted values (by the best model) for all target variables versus measured N contents (predictions for samples without N measurements are not shown). Lines and shaded areas are LOESS smoothers and 95% confidence intervals.

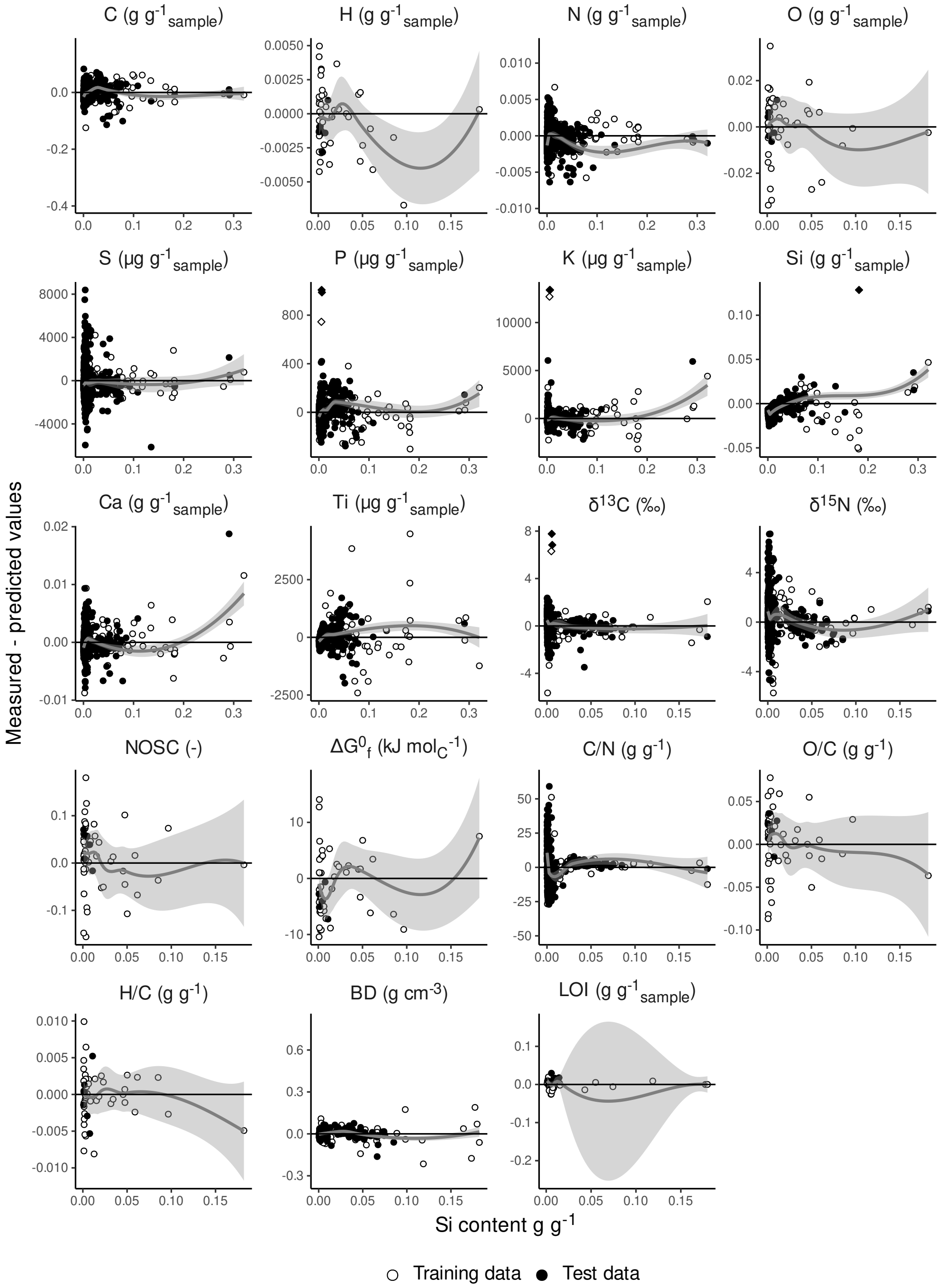

Figure S18: Measured minus predicted values (by the best model) for all target variables versus measured Si contents (predictions for samples without Si measurements are not shown). Lines and shaded areas are LOESS smoothers and 95% confidence intervals.

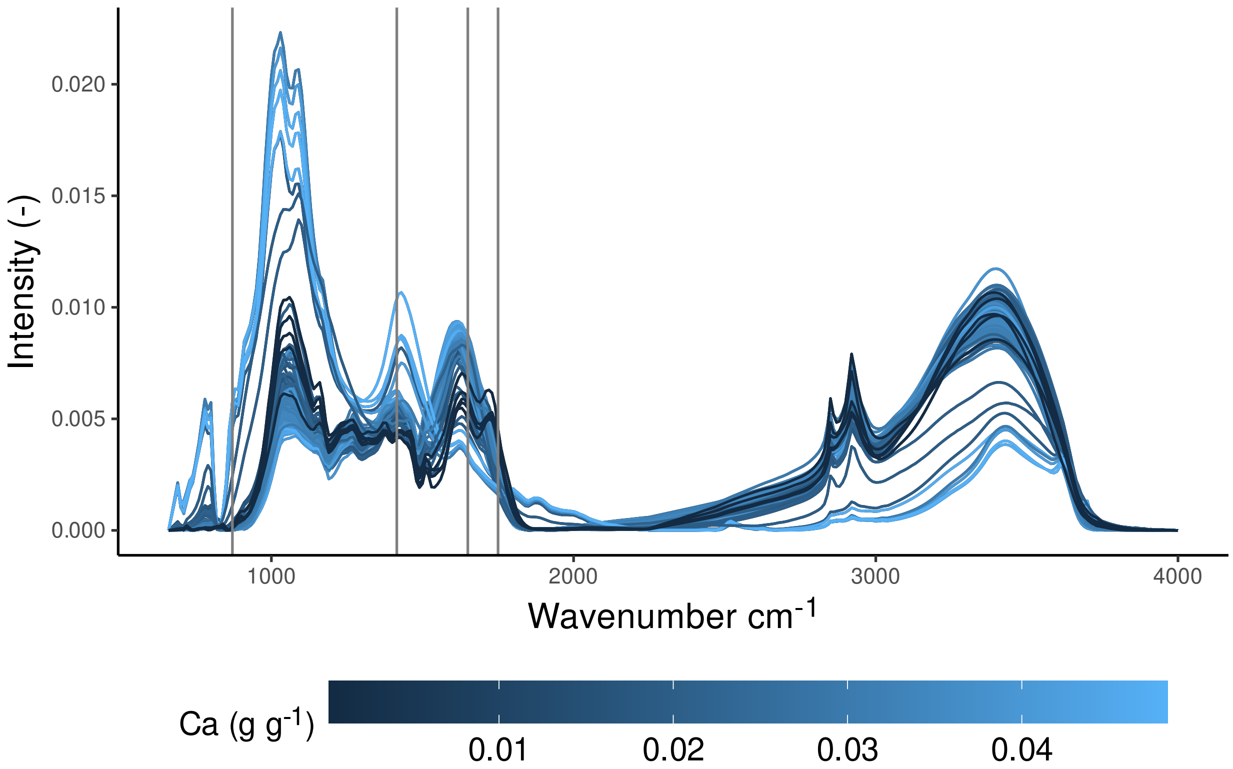

Figure S19: Plot of spectra of samples with Ca content > 0.015 g g^{-1} and for five samples with Ca content > 0.0005 g g^{-1}. Spectra with large Ca and small organic matter content (indicated by presence of large peaks caused by silicates around 1100 and 2000 cm^{-1}, e.g., Parikh et al. (2014)) have large peaks caused by carbonates (871 and 1415 cm^{-1}, vertical lines) (Tatzber et al., 2007). Spectra with large Ca and large organic matter content (indicated by large peaks from aliphatics (around 2900 cm^{-1})) have large carboxylate peaks (around 1650 cm^{-1} (Ellerbrock and Gerke, 2021), vertical line). Spectra with small Ca and large organic matter content have peaks caused by carboxyls (protonated carboxylates) (around 1750 cm^{-1} (Ellerbrock and Gerke, 2021)).

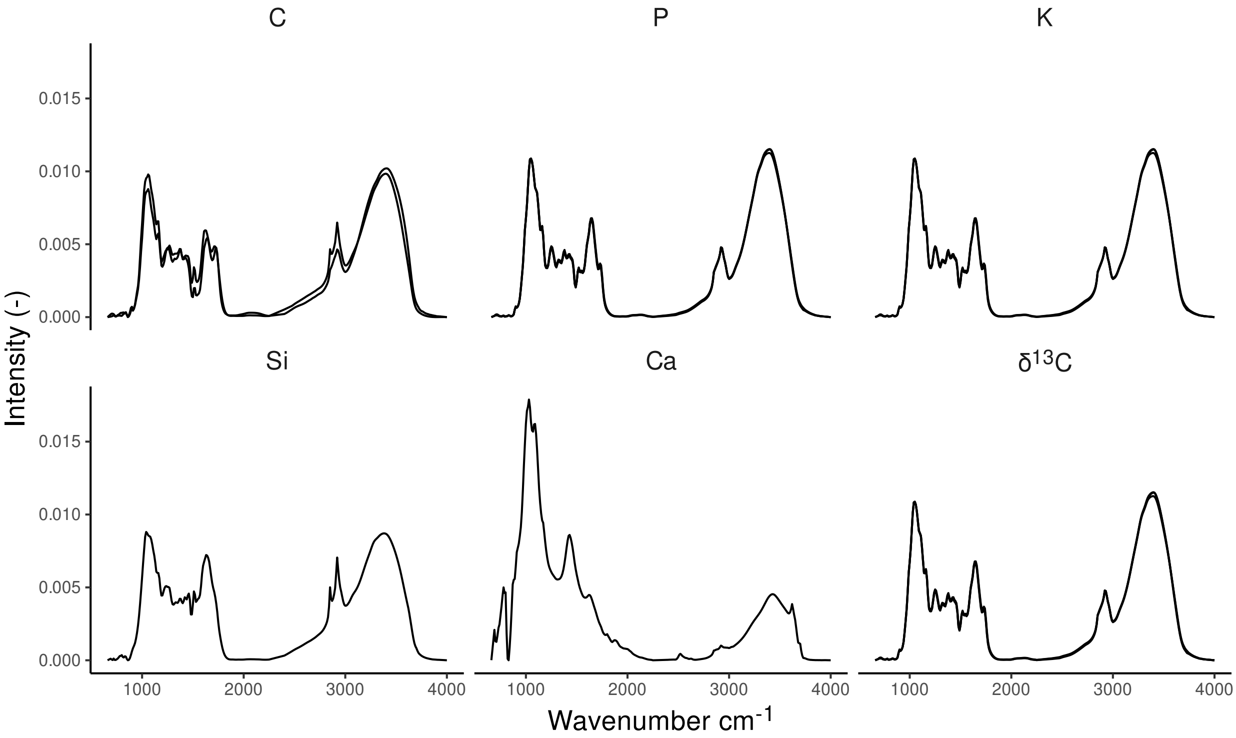

Figure S20: Plot of spectra for observations labelled as outliers in 2 for each target variable. Note that outliers are identical for P, K, and δ^{13}C (*J. effusus* samples from a short-term fertilization experiment (Agethen and Knorr, 2018)).

S5 Model coefficients

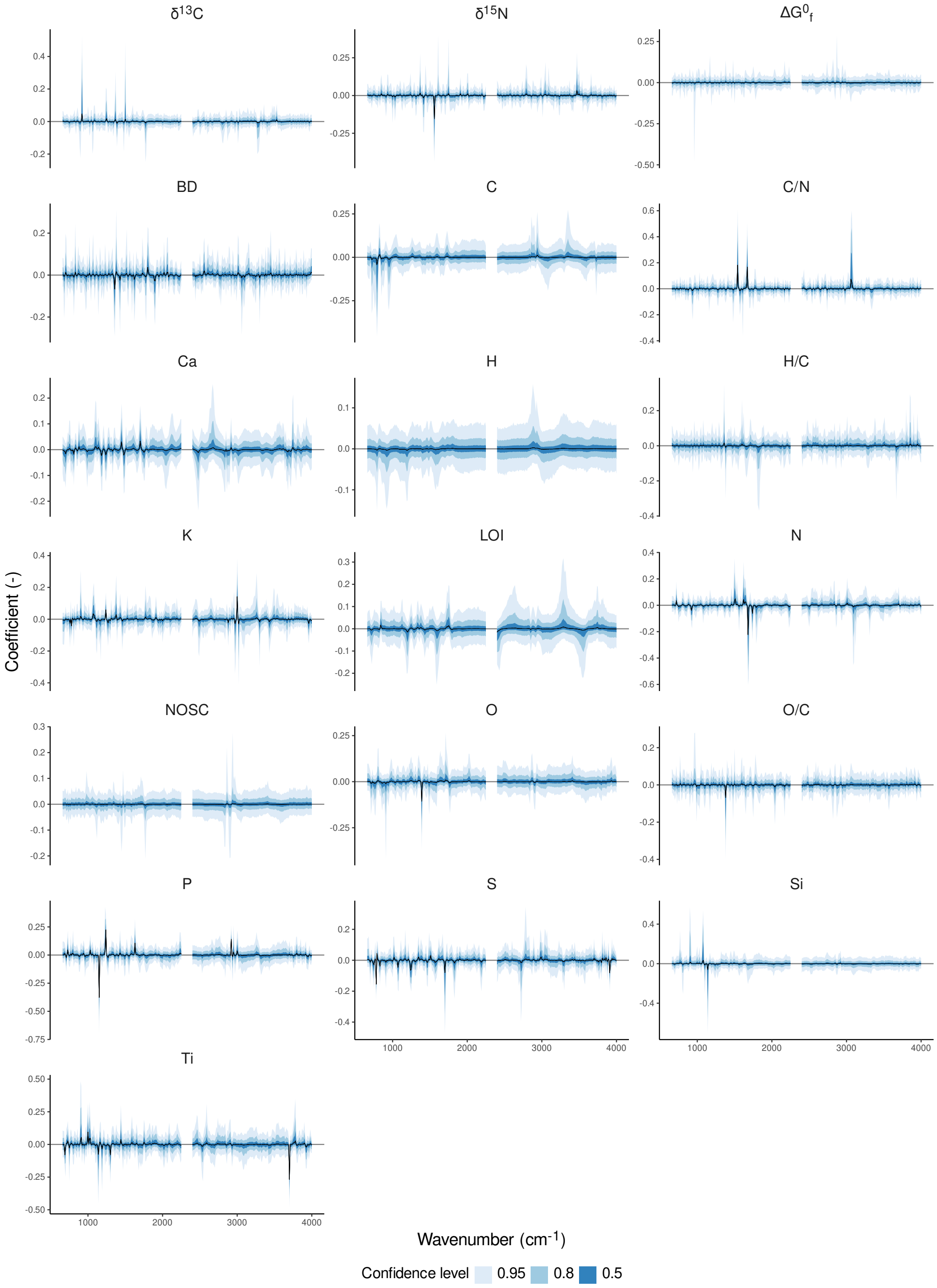

Figure S21: Model coefficients versus wavenumber values of the predictor variables for the best models (see Tab. 2 in the main text). The line is the median coefficient value and shaded areas are confidence intervals with significance level given in the legend.

Table S3: Selected coefficients (slopes) for the best models (all with Pr(slope $> 0) \geq 0.9$ or Pr(slope $< 0) \geq 0.9$) and assignment of the wavenumber values to possible molecular structures. Assignments of moelcular structures to wavenumbers are from Stuart (2004), Kubo and Kadla (2005), Schmidt et al. (2006), Tatzber et al. (2007), Parikh et al. (2014), and Workman (2016).

Variable	Wavenumber	Coefficient	Molecular structures
O	1390	-0.02 (-0.07, 0)	C–H bending (alkanes, aromatic), C=O stretch (carbonates), C-S stretch
S	780	-0.29 (-0.45, -0.11)	aromatic C-H bending (3-substitued), alkene C-H bending
	790	0.08 (-0.01, 0.21)	aromatic C-H bending (3-substitued), alkene C-H bending
	1240	-0.12 (-0.3, 0.01)	C–O stretching (carboxyls), P–O stretching, P=O stretching
	3910	-0.15 (-0.34, 0)	S=O stretch (sulfones), O-H bend (alcohols)
P	1150	-0.31 (-0.53, -0.03)	SO_2 symmetric stretching, C–O stretching (carbohydrates), P-O stretching, O-H bend
	1240	0.18 (0.01, 0.29)	C–O stretching (carboxyls), P–O stretching, P=O stretching
	1630	0.09 (0, 0.23)	C=C stretching (alkene, aromatic), C=O stretching (amide, keton)
	2920	0.12 (0.03, 0.2)	methylene C–H stretching (alkane)
K	780	-0.08 (-0.25, 0.01)	aromatic C-H bending (3-substitued), alkene C-H bending
	1240	0.12 (0, 0.3)	C–O stretching (carboxyls), P–O stretching, P=O stretching
	3000	0.29 (0, 0.68)	C-C stretching and C–H stretching (aromatic)
Ti	690	-0.1 (-0.22, 0)	C-S stretching, aromatic C-H bending
	3700	-0.35 (-0.59, -0.07)	O–H stretching of weakly bonded OH groups (amorphous cellulose, phenolics, silicates)
δ^{15}N	1560	-0.19 (-0.49, 0.01)	N–H bending and C-N stretching (amide), C=O stretching (keton, carboxylate), C-H bend (aromatics)
C/N	1670	0.07 (0, 0.19)	C=O stretching (amide, keton, quinones), C-H bend (aromatic)

References

310 Agethen, S. and Knorr, K.-H.: *Juncus Effusus* Mono-Stands in Restored Cutover Peat Bogs – Analysis of Litter Quality, Controls of Anaerobic Decomposition, and the Risk of

Secondary Carbon Loss, Soil Biology and Biochemistry, 117, 139–152, https://doi.org/10.1016/j.soilbio.2017.11.020, 2018.

Battley, E. H.: An Empirical Method for Estimating the Entropy of Formation and the Absolute Entropy of Dried Microbial Biomass for Use in Studies on the Thermodynamics of Microbial Growth, Thermochimica Acta, 326, 7–15, https://doi.org/10.1016/S0040-6031(98)00584-X, 1999.

Clymo, R. S.: The Limits to Peat Bog Growth, Philosophical transactions of the Royal Society of London. Series B, Biological sciences, 303, 51, 1984.

Dale, J., Shock, E., Macleod, G., Aplin, A., and Larter, S.: Standard Partial Molal Properties of Aqueous Alkylphenols at High Pressures and Temperatures, Geochimica et Cosmochimica Acta, 61, 4017–4024, https://doi.org/10.1016/S0016-7037(97)00212-3, 1997.

Dick, J. M.: CHNOSZ: Thermodynamic Calculations and Diagrams for Geochemistry, Frontiers in Earth Science, 7, 180, https://doi.org/10.3389/feart.2019.00180, 2019.

Ellerbrock, R. H. and Gerke, H. H.: FTIR Spectral Band Shifts Explained by OM–Cation Interactions, Journal of Plant Nutrition and Soil Science, 184, 388–397, https://doi.org/10.1002/jpln.202100056, 2021.

Gnatowski, T., Ostrowska-Ligęza, E., Kechavarzi, C., Kurzawski, G., and Szatyłowicz, J.: Heat Capacity of Drained Peat Soils, Applied Sciences, 12, 1579, https://doi.org/10.3390/app12031579, 2022.

Helgeson, H. C.: Summary and Critique of the Thermodynamic Properties of Rock-Forming Minerals, Kline Geology Laboratory Yale University, New Haven, 1978.

Helgeson, H. C., Owens, C. E., Knox, A. M., and Richard, L.: Calculation of the Standard Molal Thermodynamic Properties of Crystalline, Liquid, and Gas Organic Molecules at High Temperatures and Pressures, Geochimica et Cosmochimica Acta, 62, 985–1081, https://doi.org/10.1016/S0016-7037(97)00219-6, 1998.

Helgeson, H. C., Richard, L., McKenzie, W. F., Norton, D. L., and Schmitt, A.: A Chemical and Thermodynamic Model of Oil Generation in Hydrocarbon Source Rocks, Geochimica et Cosmochimica Acta, 73, 594–695, https://doi.org/10.1016/j.gca.2008.03.004, 2009.

Hilsenrath, J., Benedict, W. S., Fano, L., Hoge, H. J., masa, J. F., Nuttall, R. L., Touloukian, Y. S., and Woolley, H. W.: Circular of the Bureau of Standards No. 564: Tables of Thermal Properties of Gases Comprising Tables of Thermodynamic and Transport Properties of Air, Argon, Carbon Dioxide, Carbon Monoxide Hydrogen, Nitrogen, Oxygen, and Steam, Tech. Rep. NBS CIRC 564, National Bureau of Standards, Gaithersburg, MD, https://doi.org/10.6028/NBS.CIRC.564, 1955.

Kubo, S. and Kadla, J. F.: Hydrogen Bonding in Lignin: A Fourier Transform Infrared Model Compound Study, Biomacromolecules, 6, 2815–2821, https://doi.org/10.1021/bm050288q, 2005.

LaRowe, D. E. and Dick, J. M.: Calculation of the Standard Molal Thermodynamic Properties of Crystalline Peptides, Geochimica et Cosmochimica Acta, 80, 70–91, https://doi.org/10.1016/j.gca.2011.11.041, 2012.

LaRowe, D. E. and Helgeson, H. C.: Biomolecules in Hydrothermal Systems: Calculation of the Standard Molal Thermodynamic Properties of Nucleic-Acid Bases, Nucleosides, and Nucleotides at Elevated Temperatures and Pressures, Geochimica et Cosmochimica Acta, 70, 4680–4724, https://doi.org/10.1016/j.gca.2006.04.010, 2006a.

LaRowe, D. E. and Helgeson, H. C.: The Energetics of Metabolism in Hydrothermal Systems: Calculation of the Standard Molal Thermodynamic Properties of Magnesium-Complexed Adenosine Nucleotides and NAD and NADP at Elevated Temperatures and Pressures, Thermochimica Acta, 448, 82–106, https://doi.org/10.1016/j.tca.2006.06.008, 2006b.

Leeper, T. J.: tabulizer: Bindings for Tabula PDF Table Extractor Library, 2018.

Linstrom, P.: NIST Chemistry WebBook, NIST Standard Reference Database 69, https://doi.org/10.18434/T4D303, 1997.

Liu, H. and Lennartz, B.: Hydraulic Properties of Peat Soils along a Bulk Density Gradient-A Meta Study, Hydrological Processes, 33, 101–114, https://doi.org/10.1002/hyp.13314, 2019.

Liu, H., Price, J., Rezanezhad, F., and Lennartz, B.: Centennial-scale Shifts in Hydrophysical Properties of Peat Induced by Drainage, Water Resources Research, 56, https://doi.org/10.1029/2020WR027538, 2020.

Morris, P. J., Davies, M. L., Baird, A. J., Balliston, N., Bourgault, M.-A., Clymo, R. S., Fewster, R. E., Furukawa, A. K., Holden, J., Kessel, E., Ketcheson, S. J., Kløve, B., Larocque, M., Marttila, H., Menberu, M. W., Moore, P. A., Price, J. S., Ronkanen, A.-K., Rosa, E., Strack, M., Surridge, B. W. J., Waddington, J. M., Whittington, P., and Wilkinson, S. L.: Saturated Hydraulic Conductivity in Northern Peats Inferred from Other Measurements, Water Resources Research, 58, https://doi.org/10.1029/2022WR033181, 2022.

O'Connor, M. T., Cardenas, M. B., Ferencz, S. B., Wu, Y., Neilson, B. T., Chen, J., and Kling, G. W.: Empirical Models for Predicting Water and Heat Flow Properties of Permafrost Soils, Geophysical Research Letters, 47, e2020GL087 646, https://doi.org/10.1029/2020GL087646, 2020.

Parikh, S. J., Goyne, K. W., Margenot, A. J., Mukome, F. N., and Calderón, F. J.: Soil Chemical Insights Provided through Vibrational Spectroscopy, in: Advances in Agronomy, vol. 126, pp. 1–148, Elsevier, ISBN 978-0-12-800132-5, https://doi.org/10.1016/B978-0-12-800132-5.00001-8, 2014.

Patel, S. A. and Erickson, L. E.: Estimation of Heats of Combustion of Biomass from Elemental Analysis Using Available Electron Concepts, Biotechnology and Bioengineering, 23, 2051–2067, https://doi.org/10.1002/bit.260230910, 1981.

Popovic, M.: Thermodynamic Properties of Microorganisms: Determination and Analysis of Enthalpy, Entropy, and Gibbs Free Energy of Biomass, Cells and Colonies of 32

Microorganism Species, Heliyon, 5, e01 950, https://doi.org/10.1016/j.heliyon.2019.e01950, 2019.

Richard, L.: Calculation of the Standard Molal Thermodynamic Properties as a Function of Temperature and Pressure of Some Geochemically Important Organic Sulfur Compounds § §This Paper Is Dedicated to Professor Harold C. Helgeson on the Occasion of His Seventieth Birthday., Geochimica et Cosmochimica Acta, 65, 3827–3877, https://doi.org/10.1016/S0016-7037(01)00761-X, 2001.

Richard, L. and Helgeson, H. C.: Calculation of the Thermodynamic Properties at Elevated Temperatures and Pressures of Saturated and Aromatic High Molecular Weight Solid and Liquid Hydrocarbons in Kerogen, Bitumen, Petroleum, and Other Organic Matter of Biogeochemical Interest, Geochimica et Cosmochimica Acta, 62, 3591–3636, https://doi.org/10.1016/S0016-7037(97)00345-1, 1998.

Ricker, W. E.: Stock and Recruitment, Journal of the Fisheries Research Board of Canada, 11, 559–623, https://doi.org/10.1139/f54-039, 1954.

Schmidt, M., Gierlinger, N., Schade, U., Rogge, T., and Grunze, M.: Polarized Infrared Microspectroscopy of Single Spruce Fibers: Hydrogen Bonding in Wood Polymers, Biopolymers, 83, 546–555, https://doi.org/10.1002/bip.20585, 2006.

Shock, E. L.: Hydrothermal Dehydration of Aqueous Organic Compounds, Geochimica et Cosmochimica Acta, 57, 3341–3349, https://doi.org/10.1016/0016-7037(93)90542-5, 1993.

Stuart, B. H.: Infrared Spectroscopy: Fundamentals and Applications, Analytical Techniques in the Sciences, John Wiley & Sons, Ltd, Chichester, UK, ISBN 978-0-470-01114-0 978-0-470-85428-0, https://doi.org/10.1002/0470011149, 2004.

Tatzber, M., Stemmer, M., Spiegel, H., Katzlberger, C., Haberhauer, G., and Gerzabek, M. H.: An Alternative Method to Measure Carbonate in Soils by FT-IR Spectroscopy, Environmental Chemistry Letters, 5, 9–12, https://doi.org/10.1007/s10311-006-0079-5, 2007.

Thornton, W.: XV. *The Relation of Oxygen to the Heat of Combustion of Organic Compounds*, The London, Edinburgh, and Dublin Philosophical Magazine and Journal of Science, 33, 196–203, https://doi.org/10.1080/14786440208635627, 1917.

Wagman, D. D., Evans, W. H., Parker, V. B., Schumm, R. H., and Halow, I.: The NBS Tables of Chemical Thermodynamic Properties. Selected Values for Inorganic and C_1 and C_2 Organic Substances in SI Units, Tech. rep., National Bureau of Standards, Washington D. C., 1982.

Wang, G., Ju, Y., Yan, Z., and Li, Q.: Pore Structure Characteristics of Coal-Bearing Shale Using Fluid Invasion Methods: A Case Study in the Huainan–Huaibei Coalfield in China, Marine and Petroleum Geology, 62, 1–13, https://doi.org/10.1016/j.marpetgeo.2015.01.001, 2015.

Whittington, P. and Koiter, A.: Evaluation of Hydro-Physical Properties along a Northern Boreal Bog Peatland Transect, https://doi.org/10.21203/rs.3.rs-4650224/v1, 2024.

Workman, J.: The Concise Handbook of Analytical Spectroscopy: Theory, Applications, and Reference Materials: Volume 4: Infrared Spectroscopy, vol. 4, WORLD SCIENTIFIC, ISBN 978-981-4508-11-7 978-981-314-952-6, https://doi.org/10.1142/8800-vol4, 2016.